



저작자표시-비영리-변경금지 2.0 대한민국

이용자는 아래의 조건을 따르는 경우에 한하여 자유롭게

- 이 저작물을 복제, 배포, 전송, 전시, 공연 및 방송할 수 있습니다.

다음과 같은 조건을 따라야 합니다:



저작자표시. 귀하는 원저작자를 표시하여야 합니다.



비영리. 귀하는 이 저작물을 영리 목적으로 이용할 수 없습니다.



변경금지. 귀하는 이 저작물을 개작, 변형 또는 가공할 수 없습니다.

- 귀하는, 이 저작물의 재이용이나 배포의 경우, 이 저작물에 적용된 이용허락조건을 명확하게 나타내어야 합니다.
- 저작권자로부터 별도의 허가를 받으면 이러한 조건들은 적용되지 않습니다.

저작권법에 따른 이용자의 권리는 위의 내용에 의하여 영향을 받지 않습니다.

이것은 [이용허락규약\(Legal Code\)](#)을 이해하기 쉽게 요약한 것입니다.

[Disclaimer](#)

이학박사학위논문

알츠하이머병 조기진단 지표로서  
자기공명영상 질감에 대한 연구

**Texture of magnetic resonance images  
as an early biomarker of  
Alzheimer's disease**

2020년 2월

서울대학교 대학원

뇌인지과학과

이 수 빈

알츠하이머병 조기진단 지표로서  
자기공명영상 질감에 대한 연구

Texture of magnetic resonance images as an  
early biomarker of Alzheimer' s disease

지도교수 김 기 응

이 논문을 이학박사학위논문으로 제출함

2019년 12월

서울대학교 대학원

뇌인지과학과

이 수 빈

이수빈의 박사학위논문을 인준함

2019년 12월

위 원 장

부위원장

위 원

위 원

위 원

권준우 (인)  
장기환 (인)  
문인영 (인)  
김의태 (인)  
김재진 (인)

# Texture of magnetic resonance images as an early biomarker of Alzheimer's disease

Advisor: Ki Woong Kim

A dissertation submitted in partial fulfillment of the  
requirement

for the degree of

**DOCTOR OF PHILOSOPHY**

to the faculty of the

Department of Brain & Cognitive Sciences

at

**SEOUL NATIONAL UNIVERSITY**

by

**Subin Lee**

Thesis Committee:

Jun Soo Kwon Kimboong Kim In-Young Yoon  
Gnitare Kim Jae-Jin Kim

## **Abstract**

# **Texture of magnetic resonance images as an early biomarker of Alzheimer's disease**

**Subin Lee**

**Department of Brain & Cognitive Sciences**

**Seoul National University Graduate School**

Alzheimer's disease (AD) is a neurodegenerative disease with currently no cure, making early detection methods crucial for early and more efficient intervention. Texture analysis is a method of quantifying various spatial patterns of signal intensities in an image, and has been proposed as a candidate early biomarker. My thesis consists of investigations of the diagnostic, prognostic, and concurrent validity of MRI texture as a novel early imaging marker of AD.

The first part of my thesis focused on investigating the feasibility of MRI texture in discriminating and predicting AD. Specifically, I constructed a composite index of texture from 5 key regions of AD pathology and tested its accuracy in the task of classifying normal vs AD subjects (AD diagnosis) and the task of classifying MCI subjects that remain MCI after 3 years vs convert to AD within 3 years (MCI-to-AD conversion prediction). I showed that composite texture can not only discriminate AD with an accuracy of over 90%, but also predict AD conversion in both

early and late stage MCI patients with an accuracy of around 80%. Additionally, the performance of texture was significantly higher than that of hippocampal volume, which is the traditionally most used measure.

The second part of my thesis examined what aspects of AD pathophysiology that MRI texture may reflect. I investigated the effects of two hallmark pathologies of AD, amyloid- $\beta$  burden and tau burden, on the texture features of five key regions early to intermediate pathological burden. I observed that, depending on the cytoarchitecture of the region, different texture features were associated with regional tau burden but not with amyloid- $\beta$  burden. Specifically, tau burden in neocortical structures showed associations with texture features entropy and contrast, while allocortical structures showed associations with texture features autocorrelation and cluster shade.

Altogether, my thesis demonstrates that MRI texture can be used as a potential early neurodegenerative marker of AD.

**Keywords:** Alzheimer's disease, MRI, texture, biomarker, neuroimaging, early detection, prediction, pathology, validation

***Student number:*** 2014-25135

## Table of Contents

<b>Abstract</b> .....	<b>iv</b>
<b>Table of Contents</b> .....	<b>vi</b>
<b>List of Figures</b> .....	<b>viii</b>
<b>List of Tables</b> .....	<b>ix</b>
<b>Abbreviations</b> .....	<b>x</b>
<b>I. Background</b> .....	<b>1</b>
1. Alzheimer’s disease .....	2
2. Early detection methods for Alzheimer’s disease .....	5
2.1. Previous literature and limitations .....	5
2.2. MRI signal intensity – an alternative approach .....	7
3. Texture analysis .....	10
3.1. What is texture? .....	10
3.2. Applications of texture analysis in medical imaging .....	11
3.3. GLCM .....	12
3.3.1. Haralick texture features .....	16
4. Purpose of my research .....	20
<b>II. Study 1: MRI texture vs MRI volume in early detection of AD</b> .....	<b>24</b>
1. Methods .....	25
1.1. Study population .....	25
1.2. MRI preprocessing .....	27
1.3. Volume analysis .....	29
1.4. Haralick texture analysis .....	29
1.5. Statistical analysis .....	30
1.5.1. Regularized logistic regression .....	31
1.5.2. ROC analysis .....	32
2. Results .....	33
2.1. AD vs NC classification .....	36
2.2. MCI-to-AD prediction .....	36

<b>III. Study 2: Pathological correlates of MRI texture in AD -----</b>	<b>40</b>
1. Methods .....	41
1.1. Study population .....	41
1.2. MRI preprocessing .....	41
1.3. Haralick texture analysis .....	44
1.4. PET analysis .....	45
1.4.1. A $\beta$ and tau accumulation .....	45
1.4.2. <i>In vivo</i> Braak staging .....	45
1.5. Statistical analysis .....	47
2. Results .....	48
2.1. Associations between MRI texture and A $\beta$ , tau burden ...	48
2.2. Comparisons of AD pathology, MRI texture and mean signal intensity among <i>in vivo</i> Braak stage group .....	50
<b>IV. Discussion -----</b>	<b>54</b>
1. Summary .....	55
2. MRI texture as an early predictor of AD .....	57
3. MRI texture as a reflection of AD pathology .....	60
4. Advantages and limitations of my study .....	65
5. Conclusion and Perspectives .....	68
<b>V. Literature Cited -----</b>	<b>69</b>
<b>Abstract in Korean -----</b>	<b>87</b>

# List of Figures

## I. Background

Figure 1. Model of dynamic biomarkers from the AD pathological cascade .....	4
Figure 2. Possible offset directions of voxel pairs in a GLCM .....	14
Figure 3. Calculation of a normalized symmetrical GLCM .....	15
Figure 4. Proposal of MRI texture as a biomarker to push the sensitivity of MRI to earlier stages .....	23

## II. Study 1

Figure 5. ROC curves of AD classification performance .....	36
Figure 6. ROC curves of prediction of MCI-to-AD progression .....	39

## III. Study 2

Figure 7. <i>In vivo</i> Braak stage group differences in neuroimaging measures .....	53
---	----

## IV. Discussion

Figure 8. Schema of texture changes according to cytoarchitecture ----	64
--	----

## List of Tables

### I. Background

Table 1. Haralick texture features computed from GLCMs -----	16
--	----

### II. Study 1

Table 2. Characteristics of the ADNI 1, ADNI 2 participants -----	28
Table 3. Model parameters for HVI, HTI, and CTI -----	35

### III. Study 2

Table 4. Characteristics of the ADNI 3 participants -----	42
Table 5. Associations of the regional texture features with regional A $\beta$ and tau burdens -----	49
Table 6. Regional A $\beta$ burden, tau burden, and texture features by <i>in vivo</i> Braak stages -----	51

## Abbreviations

<b>A<math>\beta</math></b>	Amyloid-beta
<b>AD</b>	Alzheimer's disease
<b>ADNI</b>	Alzheimer's disease neuroimaging initiative
<b>AUC</b>	Area under the (receiver operator characteristic) curve
<b>CSF</b>	Cerebral spinal fluid
<b>DTI</b>	Diffusion tensor imaging
<b>GLCM</b>	Gray-level co-occurrence matrix
<b>MCI</b>	Mild cognitive impairment
<b>MCI-P</b>	Progressive MCI
<b>MCI-PE</b>	Progressive MCI in their early stages
<b>MCI-PL</b>	Progressive MCI in their late stages
<b>MCI-S</b>	Stable MCI
<b>MRI</b>	Magnetic resonance imaging
<b>NC</b>	Normal cognition
<b>NFT</b>	Neurofibrillary tangle
<b>P-tau</b>	Phosphorylated tau
<b>PET</b>	Positron emission tomography
<b>ROC</b>	Receiver operator characteristic
<b>ROI</b>	Region of interest
<b>T</b>	Tesla
<b>T1w</b>	Longitudinal relaxation time / T1-weighted
<b>T2w</b>	Transverse relaxation time / T2-weighted
<b>T2*w</b>	Effective transverse relaxation time / T2*-weighted
<b>T-tau</b>	Total tau
<b>2D</b>	Two-dimensional
<b>3D</b>	Three-dimensional

# **I. Background**

## 1. Alzheimer's disease (AD)

Dementia is a clinical syndrome characterized by a progressive decline in memory and other cognitive domains, causing loss of abilities to perform basic activities for independent and daily living. By 2050, the prevalence of dementia worldwide is estimated to be over 135 million people, establishing it as one of the largest public health challenges (Prince et al., 2015). This is especially a growing concern for countries in which elderly populations are rapidly increasing (Kim et al., 2014; Bae et al., 2015).

AD is the most common cause of dementia, accounting for up to 80% of all dementia diagnoses (Jhoo et al., 2008; Kim et al., 2011; Kim et al., 2014; Prince et al., 2015). A progressive neurodegenerative disease, it is characterized by hallmark pathologies that include amyloid-beta ( $A\beta$ ) peptides and hyperphosphorylated tau (p-tau).  $A\beta$  are deposited extracellularly as plaques, and p-tau aggregate intracellularly as neurofibrillary tangles (NFT) (Dubois et al., 2016). Extensive research has shown that there is a long pre-dementia period in which pathophysiological hallmarks begin to accumulate in the brain, up to 20 years before the onset of clinical symptoms. Biomarkers are variables that can be measured *in vivo* and indicate specific features of disease-related pathological changes (Jack et al., 2010). As seen in **Figure 1**, the general sequence of biomarker abnormality is accumulation of cerebral  $A\beta$ , followed by increase of cerebral p-tau, and then structural changes in the brain such as hippocampal atrophy (Jack et al., 2010).  $A\beta$  and p-tau can be detected using positron emission tomography (PET) scans and cerebral spinal fluid (CSF) samples from

lumbar punctures. Hippocampal atrophy can be observed on T1-weighted structural brain magnetic resonance imaging (MRI).

AD is an irreversible disease, and despite the extensive research and clinical trials over the past few decades there is currently no established cure or treatment for the disease except for symptom-alleviating drugs such as cholinesterase inhibitors (Schneider et al., 2014). However, multimodal nonpharmacological interventions can improve cognition and quality of life, with earlier stage pre-dementia patients receiving better benefits compared to those with dementia since their cognitive plasticity and learning potential may be more intact (Han et al., 2017a; Han et al., 2017b; Kurtz et al., 2009; Li et al., 2011).

As such, early detection has large implications in delaying further progression and reducing socioeconomic burden. This makes early detection crucial and has resulted in a shift of research from AD treatment to AD early detection. Specifically, efforts have focused on studying the mild cognitive impairment (MCI) stage, which is viewed as a stage between NC and dementia. Those with MCI exhibit lower than average memory and cognitive problems while still retaining ability to perform daily life activities normally, and have a higher overall risk of developing dementia (Petersen et al., 2001). However, MCI is a very heterogeneous group, with some converting to dementia within the next 1~3 years, some never converting and remaining as MCI, some reverting to NC, and some fluctuating between MCI and NC states (Han et al., 2012; Petersen et al., 2005). Thus, identifying which MCI patients are at risk of imminent progression to

dementia constitute an important part of early detection of AD.

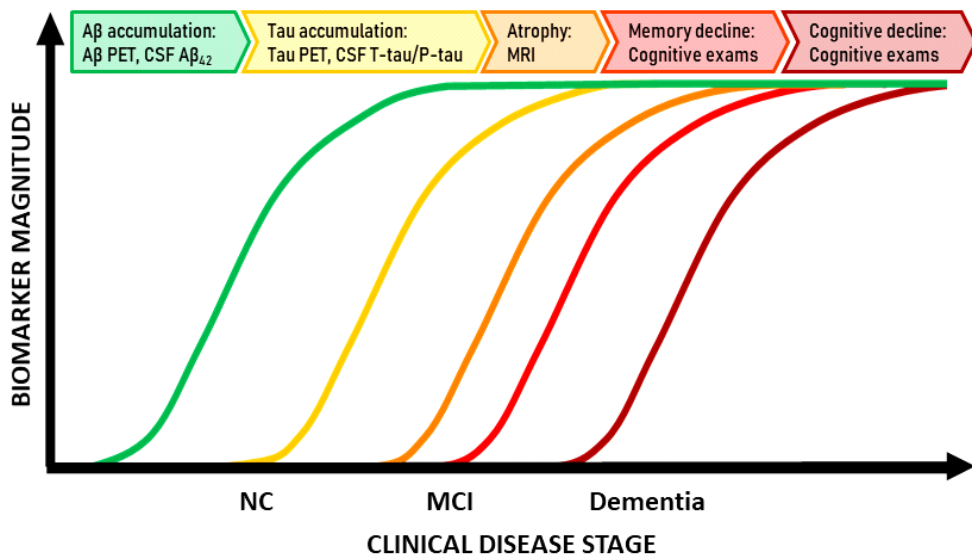


Figure 1. Model of dynamic biomarkers from the AD pathological cascade.

## 2. Early detection methods for AD

### 2.1. Previous literature and limitations

The case could be made that early detection of AD should be done in the NC stage even before the MCI stage, using biomarkers of the abnormal AD-associated proteins. However, while A $\beta$  and tau are sensitive markers of AD, the use of CSF- and PET-based A $\beta$  and tau measurements has several limitations as widely applicable early detection methods. First, lumbar punctures are invasive procedures that are painful and are not part of most clinicians' routine diagnostic workup for suspected AD. PET imaging, on the other hand, has better accuracy ([Ramusino et al., 2019](#)) and allows visualization of spatial patterns characteristic of AD. However it is a highly costly examination, includes exposure to radiation, and is not available in all clinical centers. Furthermore, in the case of A $\beta$ , while it is a hallmark pathology of AD, its presence does not always signify clinical deterioration. About 30-50% of elderly with post-mortem results of A $\beta$  presence to be classified as AD were clinically normal in their lifetimes ([Driscoll and Troncoso, 2011](#)), and many other research showed a lack of association between A $\beta$  pathology and memory decline ([Guillozet et al., 2003](#)). In the case of tau., it correlates with both atrophy and cognitive impairment better than A $\beta$  pathology ([Aschenbrenner et al., 2018](#); [Guillozet et al., 2003](#); [Nelson et al., 2012](#); [Whitwell et al., 2008](#)), but tau PET is currently used for research purposes only. Furthermore, presence of tau in the absence of A $\beta$  is classified as suspected non-Alzheimer's pathology (SNAP), suggesting that tau PETs would have to be accompanied by A $\beta$  examinations for it to

be useful early indicators of AD, which is also impractical.

MRI, on the other hand, is a non-invasive and relatively less costly method that is widely accessible (especially T1w images) because they are part of routine clinical examinations in many hospitals, which are ideal qualities of a biomarker. Furthermore, structural brain changes on MRI occur temporally after abnormal protein accumulation and before clinical manifestation, representing an accumulated effect of the protein deposits and a more direct cause of the clinical symptoms. The spatial atrophy patterns for AD are well-defined, so MRIs are often used in clinical practice to rule out other causes of the observed clinical symptoms (Frisoni et al., 2010).

Early studies established hippocampal atrophy as a very robust marker of AD disease (Albert et al., 2011; Convit et al., 1993; De Leon et al., 1996; Fox et al., 1996; Jack et al., 1992). Hippocampal atrophy is currently the most widely applied structural MRI biomarker and the golden standard for AD diagnosis (Albert et al., 2011). It is one of the first regions to be atrophied in AD, leading to the symptoms of memory decline that is characteristic of AD. However, detectable levels of atrophy occurs relatively downstream of the pathophysiological cascade compared to more microstructural changes (Jack et al., 2010), making it an insufficient early marker. Following studies proposed other regions, such as atrophy of the entorhinal cortex (Cardenas et al., 2011), medial temporal lobe (Visser et al., 2002), and enlargement of ventricles (Thompson et al., 2004). In addition, recent literature used alternative measures of atrophy, such as cortical thickness, surface area, sulcal curvature, shape, and gray matter density, and

combined them into optimal indices using machine learning methods to accurately classify AD patients from elderly with normal cognition (NC) (Casanova et al., 2011; Casanova et al., 2013; Chiang et al., 2011; Cho et al., 2012; Davatzikos et al., 2011; Fan et al., 2008; Gerardin et al., 2009; Vemuri et al., 2008). As MCI patients that later progress to dementia exhibit more AD-like characteristics compared to MCI patients that remain stable, the AD classifiers have also been applied to differentiating MCI non-converters and converters in the hopes of being able to predict which MCI patients will progress.

However, such atrophy-based structural MRI markers exhibited unsatisfactory performances in the prediction of MCI-to-AD conversion (Cuingnet et al., 2011). Theoretically, atrophy represents a stage in which substantial neuronal death and clinical progression have already occurred, and the previous studies' results suggest that volume-based information may not fully capture the early neurodegenerative process in AD. Such early processes include microscopic changes (i.e. dendritic and axonal changes, chronic inflammation, spongiform changes) that may alter tissue characteristics without necessarily causing atrophy yet (Weston et al., 2015).

## **2.2. MRI signal intensity – an alternative approach**

Microstructural changes (i.e. decreased tissue integrity, dendritic and myelin loss) have been shown to precede or add complementary value to macrostructural changes (i.e. volume loss) in the brain, making such

microscopic measures a favorable candidate for an early structural neuroimaging biomarker. These results were reported in studies using diffusion weighted imaging (Kantarci et al., 2005; Weston et al., 2015) in which the signal intensity signifies the degree of neuronal integrity (i.e. mean diffusivity of water molecules). However, diffusion weighted imaging techniques do not yet have an established role in clinical practice and are usually acquired in low spatial resolution.

Meanwhile, T1w images are included in routine clinical MRI scans and are usually acquired in high spatial resolution. T1w contrast is dependent on the properties of the underlying tissue, such as the amount of fat and water molecules, and provides excellent contrast between tissue classes (GM, WM, CSF). T1w signal intensity is known to especially be dependent on myelin content (Leuze et al., 2017), and also best explained by a weighted sum of the region's cytoarchitecture and myeloarchitecture (Eickhoff et al., 2005), which suggests the potential microscopic information of the tissue that it may contain. Furthermore, one human study found that changes in signal intensity of T1w images occur with increasing age, independently of concurrent changes in cortical thickness (Westlye et al., 2010), and other studies found that T1 relaxation time, the basis of tissue contrast in T1w images, could independently predict histological measures of neuronal density (Goubran et al., 2015; Schmierer et al., 2010). These suggest that signal itself can harbor information beyond that provided by volumetric measures.

In essence, atrophy of, for example, the GM, reflects a reduction in

the number of voxels with signal intensities that would be classified as GM on T1w images. Microstructural changes that precede atrophy would occur as signal intensity changes that are not intense enough for the voxel to be no longer classified as a certain tissue class. Detectable early microscopic changes may occur in the form of changes in signal intensity that are subtle, before it becomes drastic enough to be detected by volumetric measures. Sorensen et al. suggested a model in which normal tissue will exhibit a normal range of signal intensities while AD-affected tissue will exhibit an abnormal range of signal intensities, before atrophy occurs (Sørensen et al., 2016). As can be found in the next section, spatial patterns of signal intensities can be detected through analysis of the image's texture.

## 3. Texture analysis

### 3.1. What is texture?

Texture refers to the pattern of spatial distributions of grey-tone in a grey-scale image. Texture analysis attempts to quantify intuitive qualities described by terms such as rough, smooth, or bumpy as a function of the spatial variation in pixel or voxel (depending on the dimension of the image) intensities (In this paper, we will refer to voxels as neuroimages are 3D data). The roughness or bumpiness refers to variations in gray-levels.

Texture analysis methods can be divided into three broad groups: statistical, model-based, and convolutional/spectral based methods. In statistical measures, first order statistics are calculated from the original images and do not consider voxel relationships. Examples of first order measures include mean, variance, skewness, and kurtosis of the signal intensity. Second order statistics consider the spatial relationship between groups of two voxels in the original image (Hall-Beyer, 2000), with examples including grey-level co-occurrence matrix (GLCM) (Haralick et al., 1973), grey-level run-length matrix (GLRLM) (Kassner and Thornhill, 2010) and local binary pattern (Ojala et al., 1994). Model-based methods include the Markov random models (Goldbach et al., 1991), and convolutional/spectral-based methods include Gabor filters (Marmol, 2011), wavelets (Livens et al., 1997), fractal features (Lopes et al., 2011b), filter banks (Leung and Malik, 2001), and convolutional neural networks (LeCun and Bengio, 1995).

### **3.2. Applications of texture analysis in medical imaging**

Texture analysis was initially developed for remote sensing of terrains from aerial photographs (Darling and Joseph, 1968; Kaizer, 1955). After its first reported applications to interpretation of medical images shortly thereafter (Chien and Fu, 1974; Hall et al., 1971; Lerski et al., 1979), there has been a growing number of related studies. Conventionally, a radiologist would produce a diagnosis based on their experience and individual judgment, which can inevitably bring variability in image interpretation due to its reliance on human visual perception. Over the past decade, texture analysis has demonstrated considerable potential as an objective tool to aid in lesion segmentation, and disease detection and monitoring. Examples include segmentation, detection or staging of tumors or lesions in the brain (Christe et al., 2012; De Nunzio et al., 2011; Georgiadis et al., 2009; Hu et al., 2015; Zacharaki et al., 2009), breast (Chen et al., 2007; Shafer et al., 2011), lungs (Cherezov et al., 2019; Depeursinge et al., 2007; Depeursinge et al., 2011), liver (Lerski et al., 1979; Strzelecki and Lee, 2011) and prostate (Lopes et al., 2011a; Madabhushi et al., 2003); discrimination of lesions in multiple sclerosis (Mathias et al., 1999; Zhang et al., 2007; Zhang et al., 2008) and epilepsy (Antel et al., 2003; Bonilha et al., 2003; Jafari-Khouzani et al., 2004); and quantification of traumatic brain injury (Ahmed and Farag, 1996) from MRI, computed tomography, and ultrasound images.

Several studies that applied texture analysis to AD were also found. Various texture features of many brain regions in T1w MRI were compared among NC, MCI or AD (Chincarini et al., 2011; de Oliveira et al., 2011;

Jiang et al., 2010; Maani et al., 2015; Sørensen et al., 2016; Xia et al., 2012); used for discrimination of AD from NC (Chincarini et al., 2011; Freeborough and Fox, 1998; Sørensen et al., 2016; Zhang, 2012); and for prediction of MCI conversion to AD (Chincarini et al., 2011; Luk et al., 2018; Sørensen et al., 2016).

According to an extensive review by Depeursinge et al. (Depeursinge et al., 2014) GLCM was the most common method used in biomedical imaging applications. The Haralick texture features from GLCMs (Haralick et al., 1973) were initially developed by Haralick et al. for remote sensing, such as sea ice imagery (Soh and Tsatsoulis, 1999) and land use and forest-type classification (Ulaby et al., 1986), but it later became widely applied in the analysis of MRI scans of the liver (Mayerhoefer et al., 2010), breast cancer (Ahmed et al., 2013; Chen et al., 2007; Gensheimer et al., 2015; Nagarajan et al., 2013; Nie et al., 2008; Prasanna et al., 2014; Wu et al., 2016) and of brain tumors (Assefa et al., 2010; Eliat et al., 2012; Georgiadis et al., 2009; Hu et al., 2015; Zacharaki et al., 2009). Recently it has also been compared favorably to deep learning methods (Basu et al., 2016). The popularity of GLCM is due to its ease of interpretation and understanding. In this paper, only the GLCM will be considered and is described below.

### **3.3. Grey-level co-occurrence matrix (GLCM)**

The GLCM is a matrix that is constructed by systematically considering the spatial relation between two voxels (a reference voxel and a neighboring

voxel) at a time. The GLCM is a  $N \times N$  matrix where  $N$  is the total number of gray levels in the image or region-of-interest (ROI), and where each element of the matrix,  $P(i,j)$ , represents the probability of a voxel of value  $i$  and a voxel of value  $j$  co-occurring in the image. Construction of a GLCM typically consists of the following steps, as described below: quantization of gray levels, tabulation of the frequency of various gray-level pairs, GLCM symmetrication, and GLCM normalization.

Quantization is a common preprocessing step for GLCM analysis. The maximum number of gray levels in an image or ROI are scaled down to a certain range of discrete values (i.e. 8, 16, 32, 64, 128, or 256), rather than using the original number of gray-levels that could be, for example, few hundreds or thousands of intensities. This reduction of total number of gray levels considered for GLCM analysis is done in order to avoid sparse matrices, thereby improving statistical validity (Mahmoud-Ghoneim et al., 2008).

Next, the frequency of various voxel pairs occurring in the quantized image or ROI are tabulated into the GLCM. Voxel pairs are defined by the values of a reference voxel and neighboring voxel ( $i$  and  $j$  respectively) and the offset parameters between them (distance between the voxels as defined by  $d$ , and the direction of the neighboring voxel's location relative to the reference voxel as defined by  $(\phi, \theta)$ ). A GLCM is defined for each type of specified offset. In 2D analysis, voxel pairs of 4 offset directions ( $0^\circ$ ,  $45^\circ$ ,  $90^\circ$ ,  $135^\circ$ ) are considered, while in 3D analysis, voxel pairs of 13 offset directions are considered (**Figure 2**). In GLCM, texture calculations

are best performed on a symmetrical matrix. Hence to make the GLCM of each offset direction symmetrical, each voxel pair is counted twice: once “forwards” and once “backwards”, which interchanges the reference and neighboring voxel for the second count. Computationally, this can be achieved by adding the original GLCM with its transposed matrix, as shown in **Figure 3**.

Finally, each GLCM is normalized, by dividing each element by the total number of pairs considered. After this step, each entry in the GLCM represents the probability of the voxel pair occurring in the image. The calculation of the symmetrical, normalized GLCM is summarized in **Figure 3**.

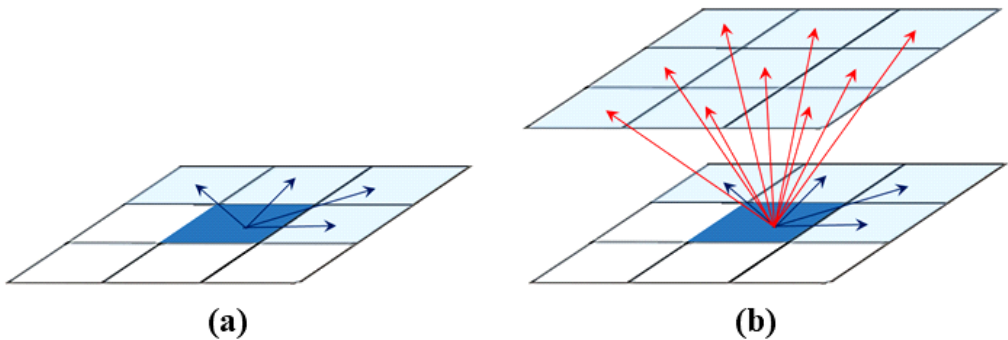


**Figure 2. Possible offset directions of voxel pairs in a GLCM.**

Examples of spatial relations between reference (dark blue) and neighboring (light blue) voxels. (a) In 2D analysis, neighboring pixels at offset directions  $(\phi, \theta) = ((0^\circ, 0^\circ), (45^\circ, 0^\circ), (90^\circ, 0^\circ), (135^\circ, 0^\circ))$  from the reference voxel are considered. (b) In 3D analysis, neighboring voxels from the adjacent slice at offset directions  $(\phi, \theta) = ((0^\circ, 45^\circ), (0^\circ, 90^\circ), (0^\circ, 135^\circ), (90^\circ, 45^\circ), (90^\circ, 135^\circ), (45^\circ, 45^\circ), (45^\circ, 135^\circ), (135^\circ, 45^\circ), (135^\circ, 135^\circ))$  are additionally considered.

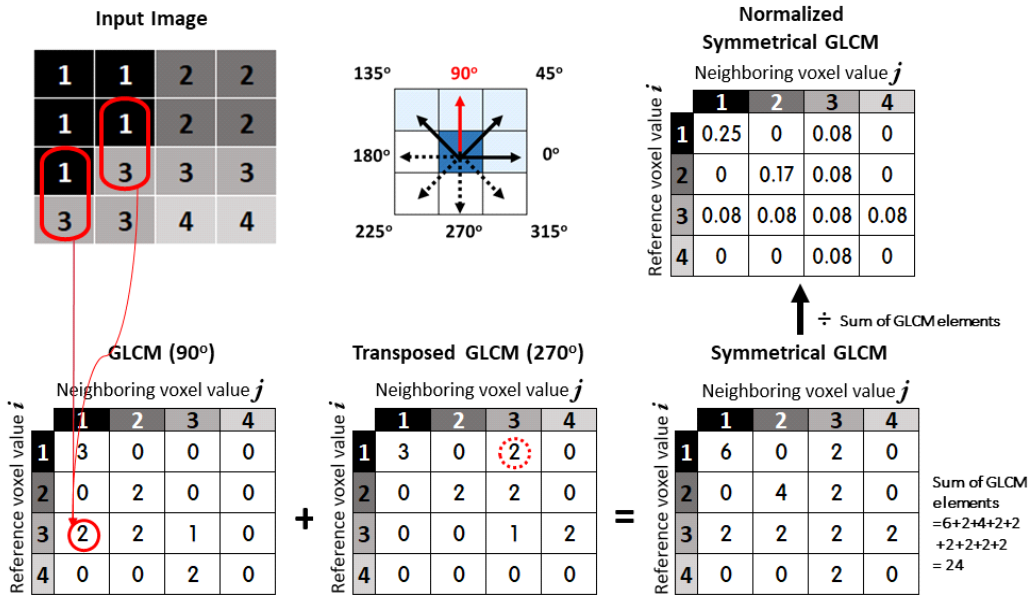


**Figure 3. Calculation of a normalized symmetrical GLCM.**

An example of how a normalized symmetrical GLCM of offset distance  $d = 1$  and direction  $90^\circ$  would be calculated. In the input image that consists of voxels of values 1 to 4, there are two instances of a reference voxel of value 3 that has a neighboring adjacent voxel of value 1 located  $90^\circ$  away from it. Thus, 2 is recorded in element (3,1) of the  $90^\circ$  GLCM (solid circle). This voxel pair can also be seen as a reference voxel of value 1 that has a neighboring voxel of value 3 located  $270^\circ$  away from it. Hence, element (1,3) of the  $270^\circ$  GLCM would also be 2 (dotted circle). In essence, the  $270^\circ$  GLCM is the transpose of the  $90^\circ$  GLCM. Summing the original and transposed GLCM produces a symmetrical GLCM, in which each possible voxel pair has been counted twice. Finally, the symmetrical GLCM is normalized by dividing each element by the sum of all elements, 24, in the matrix. Each element of the normalized GLCM now represents the probability of every combination of voxel pair occurring in the input image. For example, the probability of voxels of values 1 and 3 being vertically within each other in the input image is 8% ( $p(3,1) = p(1,3) = 0.08$ ).

### 3.3.1. Haralick texture features

From the normalized GLCM (four or thirteen depending on the dimension of analysis), an average final GLCM is computed. This final GLCM is then used as input to calculate Haralick texture features, as described in **Table 1**. Each feature represents a different aspect of the homogeneity or heterogeneity of the analyzed image.

**Table 1. Haralick texture features computed from GLCMs**

Texture feature	Equation <sup>a</sup>	Description and References
Energy	$\sum_i \sum_j p(i,j)^2$	Measures local homogeneity and represents the opposite of Entropy. Images with a constant or periodic gray level distribution give high values. Also called Angular Second Moment (Albregtsen, 2008; Alonso-Caneiro et al., 2013; Haralick et al., 1973; Soh and Tsatsoulis, 1999)
Entropy	$-\sum_i \sum_j (i+j - \mu_x - \mu_y)^3 p(i,j)$	Measures randomness of gray level distribution (spatial disorder). Solid tone image would have an entropy value of 0. (Alonso-Caneiro et al., 2013; Haralick et al., 1973; Soh and Tsatsoulis, 1999)
Dissimilarity	$\sum_i \sum_j  i-j  \cdot p(i,j)$	Measures variation of gray level pairs in an image. (Soh and Tsatsoulis, 1999)
Contrast	$\sum_i \sum_j (i-j)^2 \cdot p(i,j)$	Measures local gray level variation in an image. Heavy textures (greater dispersity in intensity values among neighboring voxels) give high values and smooth, soft textures give low values. (Haralick et al., 1973; van Griethuysen et al., 2017)

<b>Correlation</b>	$\sum_i \sum_j \frac{(ij)p(i,j) - \mu_x \mu_y}{\sigma_x \sigma_y}$	Measures the linear dependency of gray level values in the GLCM, giving a value of between 0 (uncorrelated) and 1 (perfectly correlated). (van Griethuysen et al., 2017)
<b>Homogeneity</b>	$\sum_i \sum_j \frac{1}{1 + (i - j)^2} p(i, j)$	Measures the uniformity of non-zero entries in the GLCM. Weights values by the inverse of the contrast weight. High homogeneity refers to textures that contain ideal repetitive structures (gray levels of each voxel pair are similar). Also called Inverse Difference Moment. (Alonso-Caneiro et al., 2013; Clausi, 2002; Soh and Tsatsoulis, 1999)
<b>Autocorrelation</b>	$\sum_i \sum_j (i \cdot j) p(i, j)$	Measures the magnitude of the fineness and coarseness of texture. Textures with more pairs of high gray levels give higher values (van Griethuysen et al., 2017)
<b>Cluster Shade</b>	$\sum_i \sum_j (i + j - \mu_x - \mu_y)^3 p(i, j)$	Measures skewness of the GLCM. Greater asymmetry gives higher values. (Alonso-Caneiro et al., 2013)
<b>Cluster Prominence</b>	$\sum_i \sum_j (i + j - \mu_x - \mu_y)^4 p(i, j)$	Measures skewness of the GLCM. Greater asymmetry gives higher values. (Alonso-Caneiro et al., 2013)
<b>Maximum Probability</b>	$\max_{i,j} p(i, j)$	Occurrence of the most predominant pair of neighboring intensity values. The value is expected to be high if the occurrence of the most predominant voxel pair is high. (Alonso-Caneiro et al., 2013; van Griethuysen et al., 2017)
<b>Sum of Squares</b>	$\sum_i \sum_j (i - \mu)^2 p(i, j)$	Puts relatively high weights on the elements that differ from the average

		values of P(i,j). Homogenous images give high values. Also called Variance. (Albregtsen, 2008)
<b>Sum Average</b>	$\sum_{i=2}^{2N} i p_{x+y}(i)$	Measures the relationship between co-occurences of pairs with lower intensity values and co-occurences of pairs with higher intensity values. (van Griethuysen et al., 2017)
<b>Sum Variance</b>	$\sum_{i=2}^{2N} (i - \mu_{x+y})^2 p_{x+y}(i)$	Measure of heterogeneity that places higher weights on neighboring intensity level pairs that deviate more from the mean. (van Griethuysen et al., 2017)
<b>Sum Entropy</b>	$-\sum_{i=2}^{2N} p_{x+y}(i) \log_{\square} \{p_{x+y}(i)\}$	Measures randomness of gray level distribution (spatial disorder). Sum of neighborhood intensity value differences. (Alonso-Caneiro et al., 2013; van Griethuysen et al., 2017)
<b>Difference Variance</b>	$\sum_{i=0}^{N-1} \square (i - \mu_{x-y})^2 p_{x-y}(i)$	Measure of heterogeneity that places higher weights on differing intensity level pairs that deviate more from the mean. (van Griethuysen et al., 2017)
<b>Difference Entropy</b>	$-\sum_{i=0}^{N-1} p_{x-y}(i) \log_{\square} \{p_{x-y}(i)\}$	Measures randomness/variability in neighborhood intensity value differences. (Alonso-Caneiro et al., 2013; van Griethuysen et al., 2017)
<b>Information Measure of Correlation I</b>	$\frac{HXY - HXY1}{\max\{HX, HY\}}$	Reduces to classical correlation coefficient when p(x,y) is normal. (Linfoot, 1957)
<b>Information Measure of Correlation II</b>	$\sqrt{1 - \exp_{\square} [-2(HXY2 - HXY)]}$	Reduces to classical correlation coefficient when p(x,y) is normal. (Linfoot, 1957)
<b>Inverse Difference</b>	$\sum_i \sum_j \frac{p(i,j)}{1 +  i-j /N}$	Measures local homogeneity of the image. Images with more uniform

**Normalized**

gray levels will keep the denominator low, resulting in higher value. Differences between the neighboring intensity values are normalized. (van Griethuysen et al., 2017)

**Inverse  
Difference  
Moment  
Normalized**

$$\sum_i \sum_j \frac{p(i,j)}{1 + ((i - j)/N)^2}$$

Measures local homogeneity of the image. Images with more uniform gray levels will give higher values. Weights are the inverse of Contrast weights. The square of the difference between neighboring intensity values are normalized. (Albregtsen, 2008)

**a Notations**

$p(i,j)$	$(i,j)$ th entry in a normalized gray-level co-occurrence matrix
$N$	Number of distinct gray-levels in the quantized image.
$\sum_i$ and $\sum_j$	Indicates $\sum_{i=1}^N$ and $\sum_{j=1}^N$ , respectively.
$p_x(i)$	Indicates $\sum_{j=1}^N p(i,j)$ ; $i$ th entry in the marginal-probability matrix obtained by summing the rows of $p(i,j)$ .
$p_x(j)$	Indicates $\sum_{i=1}^N p(i,j)$
$p_{x+y}(k)$	Indicates $\sum_{i=1}^N \sum_{j=1}^N p(i,j)$ , $k = 2, 3, \dots, 2N$ . $i+j=k$
$p_{x-y}(k)$	Indicates $\sum_{i=1}^N \sum_{j=1}^N p(i,j)$ , $k = 0, 1, \dots, N-1$ $ i-j =k$
$\mu_x, \mu_y, \sigma_x, \sigma_y$	means and standard deviations of $p_x$ and $p_y$
HXY	$-\sum_i \sum_j p(i,j) \log(p(i,j))$ , where HX and HY are entropies of $p_x$ and $p_y$ .
HXY1	$-\sum_i \sum_j p(i,j) \log\{p_x(i)p_y(j)\}$
HXY2	$-\sum_i \sum_j p_x(i)p_y(j) \log\{p_x(i)p_y(j)\}$

## 4. Purpose of my research

To summarize, identifying those at risk of imminent progression to dementia is crucial for timely intervention and effective treatment. For this, T1w MRI is an ideal imaging modality due to its favorable practical advantages. However, its usefulness in early detection of AD will rely on finding MRI measures that capture earlier parts of the neurodegenerative process than current volumetric measures can. The working hypothesis of previous studies of texture analysis in AD proposes that the accumulated effect of A $\beta$ s and NFTs is detectable on MRI prior to atrophy, as changes in the statistical distribution of the image signal intensities (Sørensen et al., 2016).

Regarding this hypothesis, increasingly emerging literature have demonstrated the potential of T1w MRI texture for detection of AD. Early studies reported significant group differences in various texture features or combinations among NC, MCI, and AD groups in the hippocampus, medial temporal lobe, thalamus, and corpus callosum (Chincarini et al., 2011; de Oliveira et al., 2011; Jiang et al., 2010; Maani et al., 2015; Sørensen et al., 2016; Xia et al., 2012). Later studies reported that individual texture features as well as composite texture indices combined using machine learning could discriminate AD from NC with good accuracy (Chincarini et al., 2011; Feng et al., 2011; Freeborough and Fox, 1998; Luk et al., 2018; Nanni et al., 2019; Sørensen et al., 2016), and that texture could provide information complementary to that of volume (Simões et al., 2012, Sørensen et al., 2016). However, there is insufficient literature on the validity of texture as an earlier predictor compared to the current golden standard, and none have

yet investigated what aspects of AD that texture reflects.

There remain several issues to address. First, the theoretical value of texture lies in being able to detect changes earlier than that of volume, but only one study has statistically compared the predictive performance of texture to that of volume (Sørensen et al., 2016). Second, the same study only looked at the predictability of texture on a heterogeneous group of MCI patients with mixed time to progression (included both early and late stage MCI patients), leaving it unclear whether the predictive performance of texture was due to its sensitivity in earlier stage MCI patients or due to merely a large sample size mixed with early and late stage MCI patients. It is also worth noting that the reported predictive performances of texture are about  $AUC = 0.74$ , which is average, so investigating its performance in early and late stages separately will elucidate its full potential sensitivity. Third, most previous texture studies investigated only the hippocampus or medial temporal regions, which is reasonable since they are sites of earliest neurodegeneration, but other regions that accumulate pathology that precede atrophy may be able to increase the sensitivity of texture. The precuneus and posterior cingulate cortex (PCC) are regions of earliest and heaviest A $\beta$  accumulation, considerable tau accumulation, and of early neuronal dysfunction/glucose hypometabolism and atrophy (Choo et al., 2010; Maarouf et al., 2014; Mattsson et al., 2019; Palmqvist et al., 2017; Yokoi et al., 2018). The early involvement of these regions in various types of early AD pathology make them potentially valuable candidates for early detection using texture analysis. Thus, adding texture from these regions may add early predictive value. Lastly, despite the increasing number of studies, there

is still a lack of fundamental understanding of the neuropathologic and biological correlations between AD-affected brain tissue and MRI texture analysis. Understanding how AD pathology can change texture will be critical in confirming the validity of texture for AD detection. Only one mouse study thus far has reported an association between MRI texture and NFT ([Colgan et al., 2017](#)), and there have been no investigations on the human brain yet.

In my research, I examine the long-held hypothesis that MRI texture can be used to detect subtle abnormalities in the signal intensity distribution in AD pathology-affected brains, and that as such will be able to predict AD earlier than current volumetric-based measures. To this end, I conducted two studies.

In the first study, I first investigated the validity of MRI texture as a marker that can predict progression to AD in MCI patients at an earlier stage compared to MRI volume. I constructed a composite marker using texture features from the hippocampus, as well as from the precuneus and PCC additionally, and compared their predictive performance with that of hippocampal volume, which is the current golden standard of AD ([Albert et al., 2011](#)). The comparison was done separately on early stage and late stage progressive MCI patients.

In the second study, I then investigated the associations between MRI texture and AD pathological burden in regions of early to intermediate change in AD. Based on reports that T1 signal intensity is determined by a weighted sum of the region's cytoarchitecture and myeloarchitecture ([Eickhoff](#)

et al., 2005), I hypothesized that  $A\beta$  and/or tau accumulation will be associated with T1w brain MRI texture, and that the textural changes will differ based on the region's cytoarchitecture. To test this, I examined the effects of regional  $A\beta$  and tau burden on regional texture features, as well as how texture values change with increasing AD pathology, which was measured via *in vivo* Braak stages (Scholl et al., 2016).

Altogether, I hypothesized that T1w MRI texture can be used as a novel AD neuroimaging marker that can advance the sensitivity of MRI to earlier stages of the disease.

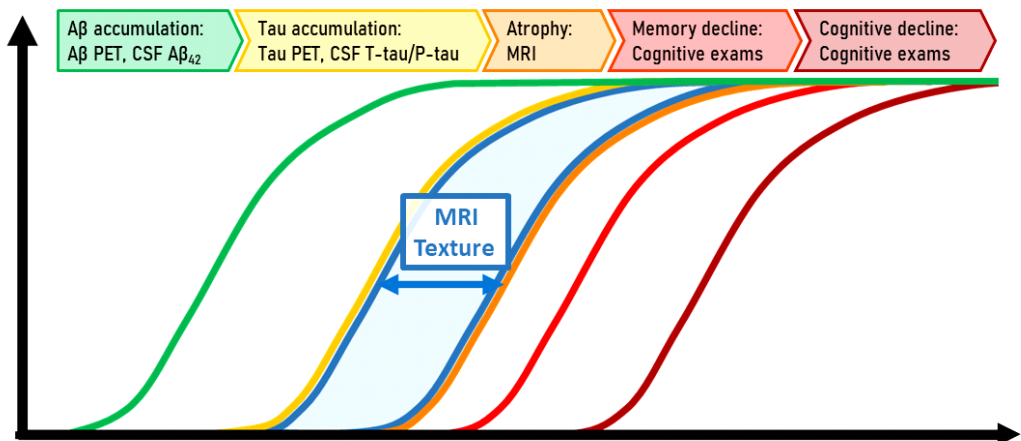


Figure 4. Proposal of MRI texture as a biomarker to push the sensitivity of MRI to earlier stages

**II. Study 1:**  
**MRI texture vs MRI volume**  
**in early detection of AD**

# 1. Methods

## 1.1. Study population

We obtained MRI scans for constructing a development dataset, validation dataset, and prediction dataset from the Alzheimer's Disease Neuroimaging Initiative (ADNI) database ([adni.loni.usc.edu](http://adni.loni.usc.edu)). For up-to-date information, see [www.adni-info.org](http://www.adni-info.org). The ADNI was approved by the institutional review board at each site, and all participants gave their written consent. Diagnostic criteria for the participants in ADNI are as follows. In terms of subjective memory complaints, NC subjects had none, while MCI and AD patients had to have complaints. The Mini-Mental State Examination (MMSE) score range (maximum score 30) for NC and MCI subjects was 24-30, and for AD was 20-26, inclusive. On the Clinical Dementia Rating (CDR) scale (maximum score 3), the score was 0 for NC subjects, was 0.5 with a mandatory requirement of the memory box score being 0.5 or greater for MCI patients, and was 0.5 or 1 for AD patients. For the memory criterion, delayed recall of 1 paragraph from the Logical Memory II subscale of the Wechsler Memory Scale-Revised (maximum score 25) was used with the following cut-off scores based on education level: for NC subjects,  $\geq 9$  was used for 16 years of education,  $\geq 5$  for 8-15 years of education, and  $\geq 3$  for 0-7 years of education; for MCI and AD patients,  $\leq 8$ ,  $\leq 4$ , and  $\leq 2$  were used for 16, 8-15, and 0-7 years of education, respectively. Furthermore, AD patients selected were those who met the NINCDS/ADRDA (National Institute of Neurological and Communicative Disorders and Stroke and the Alzheimer's Disease and Related Disorders Association) criteria for probable AD ([Black et al., 1994](#)).

We constructed the development dataset to develop indices of hippocampal volume, hippocampal texture, and a composite texture of hippocampus, precuneus, and PCC for discriminating AD from NC. The development dataset consisted of baseline or screening 3T T1w MRI scans of 145 mild AD patients and 121 NC who participated in the ADNI 2 and completed follow-up evaluations for 2 years or longer. We chose to use ADNI 2 data because they all consisted of 3T MR images, while the majority of ADNI 1 data consisted of 1.5T MR images, in which the lower signal-to-noise ratio could act as an artefact in texture analysis (Larroza et al., 2016). Additionally, we only included NC controls who maintained a NC diagnosis and a CDR Sum of Boxes score (CDR-SB) of 0 from baseline to at least 2-years of follow-up, to ensure that potentially preclinical AD subjects are not included as controls.

For the independent validation dataset, we utilized 3T images of 34 AD and 27 NC from the ADNI 1 database, with the same criteria as the development dataset. This dataset was used as external validation of AD vs NC classification performance of the three MRI indices.

We then constructed the prediction dataset to test the predictive validity for MCI-to-AD conversion of the indices developed from the development dataset. This was constructed using the baseline 3T T1w MRI scans of 194 MCI patients who participated in the ADNI 2. Among the 194 MCI patients, 113 did not progress to AD for at least 3 years since baseline assessment (stable MCI, MCI-S), and 81 progressed to AD within 3 years (progressive MCI, MCI-P). In the MCI-P group, 41 progressed to AD between 12 months to 36 months after baseline evaluation (early stage

MCI-P, MCI-PE) and 41 progressed to AD within the first 12 months since baseline evaluation (late stage MCI-P, MCI-PL). We assumed that the longer time for MCI-to-AD conversion represents patients who are in earlier stages of the disease.

Demographic and clinical characteristics of the participants are summarized in **Table 2**.

## **1.2. MRI preprocessing**

We used scanner-specific, optimally preprocessed 3T T1w MRI scans (e.g. gradient non-linearity correction, B1 non-uniformity correction, histogram peak sharpening) downloaded from the ADNI database (details can be found in [adni.loni.usc.edu](http://adni.loni.usc.edu)). We then resliced the original images to isovoxels ( $1 \times 1 \times 1 \text{mm}^3$ ) and used FreeSurfer 5.3.0 ([surfer.nmr.mgh.harvard.edu/](http://surfer.nmr.mgh.harvard.edu/)) to obtain subject-specific masks of brain regions as defined by the Desikan-Killiany atlas ([Desikan et al., 2006](#)). Briefly, this procedure involved motion correction of the T1w images, removal of non-brain tissue ([Ségonne et al., 2004](#)), automated Talairach transformation, segmentation of subcortical white matter and deep gray matter structures ([Fischl et al., 2002](#); [Fischl et al., 2004a](#)), intensity normalization ([Sled et al., 1998](#)), tessellation of the gray matter white matter boundary, automated topology correction ([Fischl et al., 2001](#); [Ségonne et al., 2007](#)), and surface deformation following intensity gradients ([Dale and Sereno, 1993](#); [Dale et al., 1999](#); [Fischl and Dale, 2000](#)). Once the cortical models are complete, registration to a spherical atlas ([Fischl et al., 1999](#)), and parcellation of the cerebral cortex into units with respect to gyral and sulcal structure ([Desikan et al., 2006](#); [Fischl et al.,](#)

**Table 2. Characteristics of the Development, Validation, and Prediction dataset subjects**

	Development Dataset			Validation Dataset			Prediction Dataset				Post hoc†
	NC (N = 121)	AD (N = 145)	<i>p</i> value*	NCv (N = 27)	ADv (N = 34)	<i>p</i> value*	MCI-S (N = 113)	MCI-PE (N = 40)	MCI-PL (N = 41)	<i>p</i> value†	
Age (years, mean ± SD)	73.4 ± 6.2	74.5 ± 8.1	0.23	75.4 ± 4.0	73.8 ± 8.1	0.31	70.2 ± 6.9	72.7 ± 7.4	71.7 ± 7.1	0.12	--
Female, N (%)	56 (46.3)	61 (42.1)	0.49	15 (55.6)	23 (67.6)	0.33	56 (49.6)	19 (47.5)	17 (41.5)	0.67	--
Education (years, mean ± SD)	16.7 ± 2.6	15.8 ± 2.6	0.005	16.4 ± 2.3	14.5 ± 3.3	0.02	16.5 ± 2.7	16.3 ± 2.7	16.2 ± 2.5	0.78	--
CDR-SB score (mean ± SD)	0.0 ± 0.0	4.4 ± 1.7	<0.001	0.0 ± 0.0	4.6 ± 1.5	<0.001	1.2 ± 0.7	1.9 ± 1.0	2.6 ± 0.8	<0.001	MCI-S <MCI-PE < MCI-PL
MMSE score (mean ± SD)	29.1 ± 1.2	23.1 ± 2.1	<0.001	29.1 ± 0.8	21.9 ± 3.3	<0.001	28.2 ± 1.7	27.4 ± 1.7	26.9 ± 2.0	<0.001	MCI-S > MCI-PE, MCI-PL

Abbreviations: SD = standard deviation; NC = normal cognition; AD = dementia due to Alzheimer’s disease; MCI-S = stable MCI patients who remained did not progress to dementia within 3 years from baseline evaluation; MCI-PE = early MCI patients who progressed to dementia from 1~3 years after baseline evaluation; MCI-PL = late MCI patients who progressed to dementia within 1 year after baseline evaluation; CDR-SB = clinical dementia rating scale sum of boxes score; MMSE = mini-mental state examination.

\* Student t-test or  $\chi^2$  test.

† One-way analysis of variance or  $\chi^2$  test, with Bonferroni post hoc comparison

2004b). For each subject we mapped their brain parcellation mask from FreeSurfer space to the isovoxel, native space and extracted 3 ROI masks (bilateral gray matter of the precuneus, PCC, and hippocampus). The ROI masks are results of collapsing the left-hemisphere and right-hemisphere ROI masks into one bilateral mask. We visually checked for any segmentation or registration errors by overlaying each subject's native-space transformed ROI masks on their T1w image.

### **1.3. Volume analysis**

To obtain bilateral volumes of the 3 ROIs, we summed the volumes of the left and right hemisphere ROI volumes returned by FreeSurfer.

### **1.4. Haralick texture analysis**

To obtain texture measures of the brain regions, we conducted 3D GLCM texture analysis (Haralick et al., 1973) in each ROI. We chose the GLCM method not only because of its predominant use in previous AD texture literature, but also for its relative ease of interpretation compared to other texture methods and its reliance on the relative rather than absolute value of voxels in an image (second-order vs first-order texture), which would make it less susceptible to interscan variability in signal intensity values. Prior to texture analysis, we first extracted ROI images with the original signal intensity values from each subject's T1w image and normalized the signal intensity within each ROI image by applying the  $\pm 3\sigma$  normalization method. This method, which is the recommended normalization procedure for texture analysis, removes any voxels with intensity values beyond the  $[\mu$

-  $3\sigma$ ,  $\mu + 3\sigma$ ] range (Collewet et al., 2004), thereby guarding against measurement error due to partial volume effects. Since texture analysis is in general assumed to be conducted over a homogenous area (ie. gray matter only), applying this method allows us to exclude any voxels affected by from neighboring cerebrospinal fluid (CSF) or white matter. We then performed quantization by rescaling all gray-level values within each histogram-normalized ROI image to a uniform range of 64. We found 64 to be an appropriate quantization level because the histogram-normalized ROIs typically had few hundreds of gray levels. Next, in each ROI, we computed 3D GLCMs for voxel pairs of within  $d = 1$  of each other in 13 possible directions (Ortiz et al., 2013). In this manner, spatial relations of voxels from not only the same slice but adjacent slices can also be considered. Twenty-one texture features were then calculated for each of the 13 GLCMs and averaged. These averaged texture features are obtained from each of the ROIs, yielding 63 texture features total (21 features/region x 3 regions). Texture analyses were performed in subject space and did not involve spatial normalization, to avoid introducing any artefacts or distorting original signal intensities.

## **1.5. Statistical analysis**

We compared continuous variables using independent samples t-test or one-way analysis of variance (ANOVA), and categorical variables using chi-square test. We considered 2-sided  $p$  below 0.05 as statistically significant.

We derived model parameters for hippocampal volume, hippocampal

texture and composite texture that discriminate AD from NC in the development dataset using logistic regression. For the hippocampal volume index, we entered hippocampal volume, age, and gender as independent variables in a logistic regression discriminating between AD and NC. While the main objective of our study was to compare texture with hippocampal volume (the current structural MRI measure in AD diagnostic criteria), we also created a composite volume index with the volumes of the 3 ROIs, age, and gender.

### **1.5.1. Regularized logistic regression**

For the hippocampal and composite texture index, we found that many texture features are intercorrelated (variance inflation factor  $> 20$ ), unlike in the volume models (variance inflation factor  $< 2$ ). This multicollinearity can result in unstable model parameters as well as overfitting. Thus, we employed an additional regularization step to the logistic regression using the glmnet library ([stanford.edu/~hastie/glmnet\\_matlab/](http://stanford.edu/~hastie/glmnet_matlab/)) on Matlab (Qian, 2013). Glnet regularizes the size of the coefficients by applying a mixture of two different regularization methods – ridge regression and LASSO (least absolute shrinkage and selection operator) – and has been used successfully in other AD classification studies involving high-dimensional MRI data (Casanova et al., 2011; Casanova et al., 2012; Casanova et al., 2013). The regularized logistic regression (RLR)(Friedman et al., 2010; Kessler et al., 2015) procedure involves first optimizing the two hyperparameters  $\lambda$  and  $\alpha$ . The hyperparameter  $\lambda$  controls the amount of coefficient regularization, and  $\alpha$  (ranging from 0 to 1) controls the weight given to ridge regression ( $\alpha = 0$ ) and LASSO ( $\alpha = 1$ ). Ridge regression handles multicollinearity by

shrinking all coefficients smoothly toward 0 but retains all variables in the model, while LASSO performs both coefficient shrinking and feature selection to offer a model that is simple but can be unstable in the presence of multicollinearity. The glmnet uses an elastic net approach to optimally combine the two regularization methods to yield more stable and accurate estimates than with either one alone while maintaining model parsimony (Kessler et al., 2015).

Hyperparameter optimization is performed by repetitively conducting 10-fold cross validation on the development dataset, with various hyperparameter values. Briefly, the development dataset is divided into randomly-formed 10 subgroups with one assigned as a test set and the remaining 9 used as the training set. A model derived from the training set is applied to the test set, and this process is repeated 10 times using a different subgroup as the test set. The mean performance across the 10 test sets, which is the mean cross-validated accuracy (measured via area under the curve [AUC]), is calculated for each combination of hyperparameters  $\lambda$  and  $\alpha$ . The hyperparameter values that return the highest mean cross-validated accuracy are then used as input to RLR analysis on the whole development dataset, along with the texture features, age and gender. From here, we obtained a set of model parameters for hippocampal or composite textures.

### **1.5.2. ROC analysis**

To obtain an overall estimate of the models' AD classification performance, we conducted nested 10-fold cross validation on the development dataset,

averaged over 10 repetitions. To obtain performance externally validated AD classification and prediction scores, we applied the model parameters for texture and volume obtained from the development dataset to the data of validation dataset and prediction dataset to yield logit scores in each individual; the hippocampal volume index (HVI), hippocampal texture index (HTI), composite texture index (CTI), and composite volume index (CVI). The composite indices included measures from all 3 ROIs (precuneus, PCC, hippocampus).

We then conducted receiver operator characteristics (ROC) analyses to evaluate overall model accuracy via the AUC measure, and used DeLong tests (DeLong et al., 1988) to compare the AUCs among the HVI, HTI, and CTI for predicting MCI-to-AD conversion.

## 2. Results

The model parameters of HVI, HTI and CTI obtained from the development dataset are summarized in **Table 3**. Hyperparameter optimization in both the hippocampal texture model and composite texture model revealed that giving equal weight ( $\alpha = 0.5$ ) to both the LASSO and ridge regression methods give highest cross-validated AUC (result of 10-fold cross validation) for discriminating AD from NC (AUC = 0.920 - 0.936). Thus, the estimated model parameters for both texture models reflect a mix of balance between selection of the most relevant features and model stability. The final parameters of the texture models included the intercept and non-zero

coefficients. The hippocampal texture model included 15 out of 21 features and the composite texture model included 27 out of 63 texture features. Cluster shade, maximum probability, sum average, and information measures of correlation I were commonly chosen in all three regions. Of note is that glmnet returns coefficients in the original scale of the features, meaning that due to the various value ranges of each feature, the coefficients in Table 2 can seem fluctuous. Features with very small coefficients such as cluster shade have very high absolute values, ranging in the thousands, while features with large coefficients such as energy have very low sub-decimal values. However, during actual calculation, the features were automatically standardized before being fitted to the RLR model.

**Table 3. Model parameters for HVI, HTI and CTI**

Parameters	HVI	HTI	CTI		
			Precuneus	PCC	Hippocampus
Intercept	21.22	316.94	81.94		
Coefficients					
Volume	-0.0020	-	-	-	-
Energy	-	0	-2095.07	0	-474.31
Entropy	-	-6.95	0	0	-6.68
Dissimilarity	-	2.79	0	0	0.78
Contrast	-	-0.040	0	0	0
Inverse Difference	-	-13.16	0	0	-37.69
Correlation	-	12.49	0	0	0
Homogeneity	-	0	0	0	-21.90
Autocorrelation	-	0.0041	0	-7.49E-06	0
Cluster Shade	-	-0.0023	-0.00054	-0.00029	-0.0015
Cluster Prominence	-	-6.67E-05	0	0	-4.16E-05
Maximum Probability	-	179.93	-333.24	-428.67	-37.02
Sum of Squares	-	0	0	0	0
Sum Average	-	0	-0.063	-0.061	0.052
Sum Variance	-	5.90E-05	0	0	3.47E-05
Sum Entropy	-	0	3.16	0	0
Difference Variance	-	-0.037	0	0	0
Difference Entropy	-	4.99	0	8.22	1.97
IMC I	-	-56.30	-5.98	25.58	-58.94
IMC II	-	79.94	21.52	0	58.88
IDN	-	-375.78	0	0	-111.82
IDMN	-	0	0	0	0
Age	-0.095	-0.12	-0.11		
Gender	-0.76	-0.52	-0.45		

PCC, posterior cingulate cortex; IMC, Information Measures of Correlation; IDN, Inverse Difference Normalized; IDMN, Inverse Difference Moment Normalized

## 2.1. AD vs NC classification

Nested 10-fold cross validation of the texture indices showed an overall AUC of over 0.90. On the validation dataset, the HVI, HTI, and CTI achieved similar performance of around AUC = 0.88. Results are illustrated in **Figure 5**.

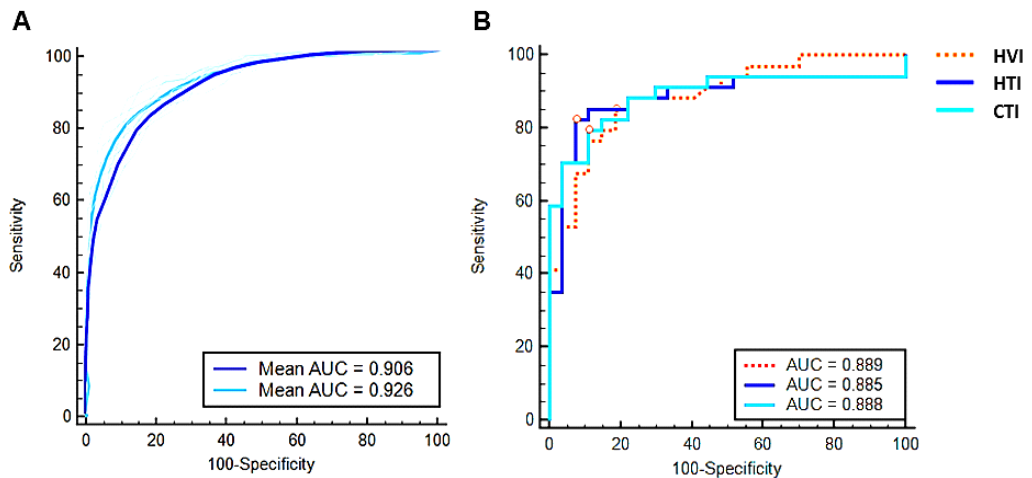


**Figure 5. ROC curves of AD classification performance.**

(A) Nested 10-fold cross validation results of HTI and CTI on the development dataset. (B) External validation results of HVI, HTI, and CTI on the independent ADNI1 3T dataset. Optimal cut-offs according to the Youden index are shown in orange circles. Abbreviations: HVI, Hippocampal Volume Index; HTI, Hippocampal Texture Index; CTI, Composite Texture Index.

## 2.2. MCI-to-AD progression prediction

The results of texture and volume on the prediction dataset are shown in **Figure 6**. In the discrimination of MCI-S from MCI-P, MCI-PE, and MCI-PL, the performance of CTI did not significantly increase from that of

HTI ( $p = 0.177, 0.272, \text{ and } 0.338$ , respectively). However, both HTI (AUC = 0.790) and CTI (AUC = 0.811) discriminated MCI-P from MCI-S better than HVI (AUC = 0.739,  $p = 0.047$  for HTI and  $p = 0.007$  for CTI). Furthermore, HTI was able to predict AD conversion marginally better than HVI in early MCI (AUC = 0.795 vs 0.726,  $p = 0.06$ ), but not in late MCI (AUC = 0.785 vs 0.753,  $p = 0.249$ ). In the case of CTI, it predicted better than HVI in both early (AUC = 0.817 vs 0.726,  $p = 0.029$ ) and late (AUC = 0.805 vs 0.753,  $p = 0.019$ ) MCI.

While our main analyses compared texture to HVI, we also conducted comparison analyses with CVI as well (not shown). In the discrimination of MCI-S from MCI-P and MCI-PE, CVI showed a non-significant increase in sensitivity compared to HVI ( $p = 0.136$  and 0.589, respectively). CTI remained more accurate than CVI in MCI-S vs MCI-P (AUC = 0.811 vs 0.769,  $p = 0.06$ ) and MCI-S vs MCI-PE (AUC = 0.817 vs 0.741,  $p = 0.027$ ). However in MCI-S vs MCI-PL, CVI showed a significant increase ( $p = 0.044$ ) from HVI, and reached performance similar to that of the CTI (AUC = 0.805 vs 0.797,  $p = 0.709$ ).

In addition, we investigated the possible impact that regularization may have on the performance of the CTI and HTI over HVI. Using forward stepwise logistic regression (no regularization) for texture resulted in a HTI model with 5 features, and a CTI model with 7 features (not shown), which is similar to the number of features for HVI (1 feature) and CVI (3 features). The non-regularized HTI and CTI remained more accurate than HVI in MCI-S vs MCI-P (AUC = 0.790 and 0.802 for non-regularized HTI and CTI respectively) and in MCI-S vs MCI-PE (AUC = 0.795 and

0.805 for non-regularized HTI and CTI respectively). In MCI-S vs MCI-PL, performance relative to HVI was similar (AUC = 0.786 and 0.799 for non-regularized HTI and CTI respectively).

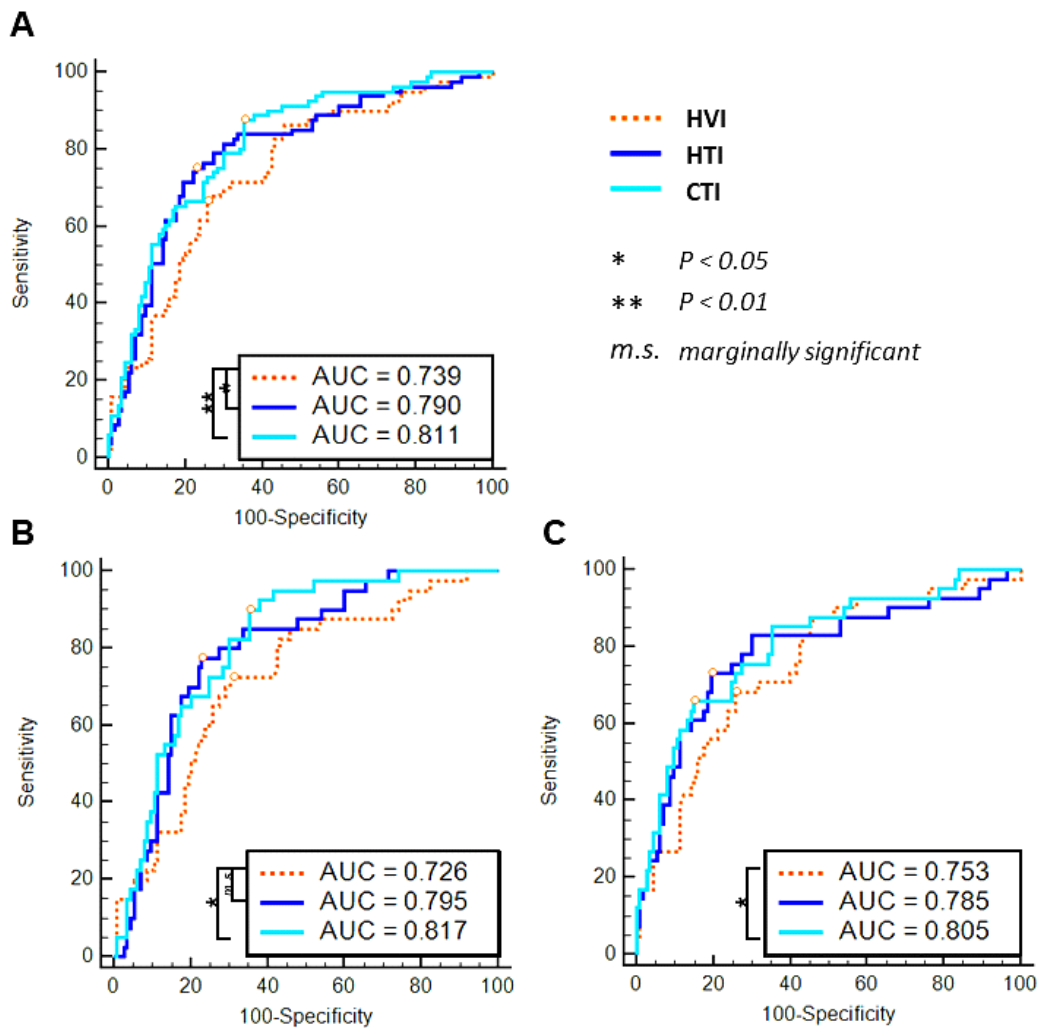


**Figure 6. ROC curves of prediction of MCI-to-AD progression.**

Comparisons of the HVI, HTI, and CTI in classification of: (A) MCI-S vs MCI-P, (B) MCI-S vs MCI-PE, and (C) MCI-S vs MCI-PL. Significance of differences in AUC between indices are indicated. Abbreviations: HVI, Hippocampal Volume Index; HTI, Hippocampal Texture Index; CTI, Composite Texture Index; MCI-S, MCI who remain stable for 3 years; MCI-P, MCI who progress to AD within 3 years; MCI-PE, early stage MCI who progress to AD 1~3 years since baseline; MCI-PL, late stage MCI who progress to AD within 1 year since baseline.

**III. Study 2:**  
**Pathological correlates of**  
**MRI texture in AD**

# 1. Methods

## 1.1. Study population

For this study, we used data of 151 participants from ADNI 3, as summarized in **Table 4**. We included subjects who had a T1w MRI obtained from a Siemens scanner, a F<sup>18</sup>-AV45 (florbetapir) PET scan, and a F<sup>18</sup>-AV1451 (flortaucipir) PET scan, all taken within 3 months of each other regardless of their clinical diagnoses. We limited our T1w images to those from one type of scanner (Siemens), because texture features are known to change substantially with differences in MRI scanner platforms ([Buch et al., 2018](#)) and the number of images obtained from Siemens MRI scanners was far larger than that of the images from GE scanners (n = 66) and Philips scanners (n = 17) in the ADNI 3.

## 1.2. MRI preprocessing

In ADNI 3, all T1w images are corrected for non-uniformity on-scanner, no longer requiring offline preprocessing. We downloaded the T1w images of each participant, resliced them to isovoxels (1 x 1 x 1 mm<sup>3</sup>), and used FreeSurfer 6.0 ([surfer.nmr.mgh.harvard.edu/](http://surfer.nmr.mgh.harvard.edu/)) to parcellate them into brain regions as defined by the Desikan-Killiany atlas. For each subject, we mapped their brain parcellation mask from FreeSurfer space to the isovoxel native space, and extracted bilateral masks for each brain region-of-interest (ROI) by combining the left- and right-hemisphere components. The ROIs chosen were the hippocampus, entorhinal cortex, posterior cingulate cortex (PCC), precuneus, and superior frontal cortex (SFC), as they are

**Table 4. Characteristics of the ADNI 3 participants**

	All	NC (N = 95)	EMCI (N = 25)	LMCI (N = 26)	AD (N = 5)
Age, mean (SD)	75.6 (7.6)	76.5 (7.7)	73.8 (6.1)	74.4 (6.2)	75.7 (7.7)
Female, %	47.7%	57.9%	20.0%	42.3%	20.0%
A $\beta$ -positive, %	19.2%	11.6%	28.0%	26.9%	80.0%
<i>In vivo</i> Braak stage, % <sup>a</sup>					
Stage 0	74.2%	85.3%	68.0%	53.8%	0.0%
Stage I-II	13.2%	10.5%	12.0%	23.1%	20.0%
Stage III-VI	12.6%	4.2%	20.0%	23.1%	80.0%
Days between T1 and AV45 scan, mean (SD)	18.7 (20.1)	19.8 (21.1)	14.8 (18.1)	18.2 (19.8)	21.6 (13.0)
Days between T1 and AV1451 scan, mean (SD)	22.5 (22.4)	22.3 (21.9)	16.3 (21.6)	27.1 (23.4)	35.8 (25.4)
Days between AV45 and AV1451 scan, mean (SD)	12.5 (16.7)	11.9 (18.1)	14.2 (16.6)	12.5 (11.1)	15.8 (15.0)

Abbreviations: NC, normal cognition; EMCI, early mild cognitive impairment; LMCI, late mild cognitive impairment; AD, Alzheimer's disease; A $\beta$ , amyloid- $\beta$ ; SD, standard deviation; AV45, florbetapir; AV1451, flortaucipir.

Means between NC, EMCI, LMCI and AD groups were compared using one-way analysis of variance for continuous variables and chi-square test for categorical variables.

<sup>a</sup> Tau PET-based (Scholl et al., 2016)

representative of regions affected by both neuropathologies from the early to late phases of AD (Braak et al., 2006; Mattsson et al., 2019), as well as consist of different cytoarchitecture, including regions ranging from the allocortex and periallocortex to the proisocortex and true isocortex. We used the bilateral masks to extract ROI images for each of the 6 regions with the original signal intensity values from each subject's T1w image.

Each ROI image of each subject were further preprocessed as previously described in **I. Background Section 3.3**, with one additional preprocessing step. After histogram normalization and before quantization, we also normalized the signal intensity value of each gray matter voxel, with respect to the mean CSF signal intensity in the lateral ventricle regions. This was done because while we limited our analyses to images from a single MRI scan platform, considerable variation in the scales can still exist across different subjects because of the session- and subject- specific optimization procedures performed during MR acquisition (Westlye et al., 2010). Rescaling using the individual's CSF value will allow us to correct for any interindividual variations in scaling factors. For quantization of each ROI image, we rescaled all signal intensity values to a uniform range of 1 to 32, as a pre-investigation of our ADNI 3 images, which have a smaller range of values than previous ADNI images, showed that a quantization level of 64 resulted in cases where no voxel values were assigned to a certain bin. This resulted in possible artefacts in the following texture analysis, whereas reducing to 32 levels solved this issue. Throughout the preprocessing process we did not perform any spatial normalization, to avoid introducing any artefacts or distorting original intensity variations.

### 1.3. Haralick texture analysis

In each preprocessed ROI image, we conducted 3D gray-level co-occurrence matrix (GLCM) analysis (Haralick et al., 1973; Ortiz et al., 2013) to extract texture features (Conners et al., 1984; Haralick et al., 1973) that characterize spatial patterns of gray-level distribution in the image. Again, we looked at voxel pairs of within  $d = 1$  of each other (directly adjacent voxels) in 13 different directions, resulting in 13 GLCMs per ROI. The average GLCM was used as input to extract Haralick texture features. Out of the twenty-one GLCM texture features available, four features (entropy, contrast, autocorrelation, and cluster shade) that uniquely characterize a different aspect of the image's signal intensity composition were selected.

Entropy reflects the randomness of spatial distribution of grey-levels without regard to the intensity of those voxels, whereas contrast reflects both the spatial distribution and the relative difference in intensities of neighboring voxels. Specifically, contrast becomes higher when neighboring voxels have very different intensities (expected in a sharp, heterogeneous image) compared to having very similar intensities (expected in a solid-tone, homogenous image). Autocorrelation reflects the overall brightness/darkness as well as fineness/coarseness of an image. Cluster shade reflects asymmetry of the proportion of relatively bright and dark intensities in the image, with the sign indicating the direction of the asymmetry (i.e. a negative value corresponds to a higher proportion of brighter voxels than darker voxels in the image, and vice versa) and the absolute value representing the magnitude of asymmetry. In total, twenty texture features (four texture

features x five ROIs) were calculated in each subject.

## **1.4. PET analysis**

### **1.4.1. A $\beta$ and tau accumulation**

To measure cerebral A $\beta$  burden and cerebral tau burden, we downloaded fully preprocessed (“Coreg, Avg, Std Img and Vox Siz, Uniform Resolution”) AV45 PET images and AV1451 PET images, respectively, from the ADNI 3 database. We used PETSurfer (Greve et al., 2016) to perform MRI-PET coregistration and calculate standardized uptake value ratios (SUVR) in each FreeSurfer-defined region, using uptake in the whole cerebellum as a reference region. The SUVR was corrected for partial volume effects via the geometric transfer matrix method. We also determined the A $\beta$  positivity of each subject based on a cortical summary SUVR score from AV45 scans (Landau et al., 2012). Briefly, this summary measure is an average of AV45 uptake from each subregion within four large regions (frontal, anterior/posterior cingulate, lateral parietal, lateral temporal), normalized to uptake from the whole cerebellum. A cut-off of 1.11 is used to determine A $\beta$  positivity.

### **1.4.2. *In vivo* Braak staging**

For comparison of texture across different stages of AD neuropathology, we divided our ADNI 3 sample into three groups based on Braak staging. We referenced the AV1451 uptake-based *in vivo* Braak staging method from a previous study (Schöll et al., 2016).

Briefly, we used weighted AV1451 average uptake measures from 3

non-overlapping composite ROIs that approximate the anatomical definitions of each Braak stage: Braak stage I/II (transentorhinal), Braak stage III/IV (limbic), and Braak stage V/VI (isocortical) (A list of regions corresponding to each stage can be found in Table S1 of Schöll and colleagues' paper). We then calculated thresholds for each Braak ROI's AV1451 uptake to assign a Braak stage to each participant, using the function *ctree* from the *party* package in R (v.3.4.3). This conditional inference tree approach embeds decision tree-structured regression models, and involves performing binary recursive partitioning using the following steps: (1) Test the global null hypothesis of independence between any input variables and the response (which may be multivariate as well), and stop if this hypothesis cannot be rejected. Otherwise select the input variable with strongest association to the response.

This association is measured by a p-value corresponding to a test for the partial null hypothesis of a single input variable and the response. (2) Implement a binary split in the selected input variable. (3) Recursively repeat steps (1) and (2).

For the cutoff score calculation, we used a subgroup (N = 113) of our sample that consists of A $\beta$ -negative cognitively normal (72 NC and 12 SMC), A $\beta$ -positive cognitively normal (7 NC and 4 SMC), and A $\beta$ -positive cognitively impaired (7 EMCI, 7 LMCI, 4 AD) individuals. This grouping was used as a response variable in the conditional inference tree analysis. In the first step, we entered the subgroup into a model classifying them based on Braak V/VI ROI uptake, which returned a suggested threshold. Subjects with a Braak V/VI ROI uptake greater than or equal to the threshold were

assigned as Braak stage V-VI. Subjects with a Braak V/VI ROI uptake less than the threshold were then entered into a model classifying them based on Braak III/IV ROI uptake. This procedure was repeated to obtain thresholds for Braak III/IV and Braak I/II ROI uptake. Based on these three thresholds, subjects in the whole dataset were assigned as Braak stage 0, I-II, III- IV, or V-VI. Cut-off scores from this subset was used to grade the *in vivo* Braak stage of the other subjects in the whole dataset (e.g. A $\beta$ -negative cognitively impaired subjects).

### **1.5. Statistical analysis**

We examined the associations of texture features with A $\beta$  burden and tau burden in each region using linear regression analyses, in which regional texture features were computed as the dependent variable, regional AV45 uptake and AV1451 uptake as the independent variables, and age and sex as covariates. While ROI volume could be a possible factor contributing to the texture features, we did not include it as a covariate because GLCM texture measures are normalized to the total number of voxels in the ROI, which would adjust for such volumetric differences. We also examined the association of mean signal intensity with A $\beta$  burden and tau burden in each region using linear regression analyses, in which regional mean signal intensities were computed as the dependent variable, regional AV45 uptake and AV1451 uptake as the independent variables, and age and sex as covariates. The mean signal intensity used here is the value derived after the  $\mu \pm 3\sigma$  normalization method and the normalization to the subject's mean ventricle signal intensity. We also compared the regional A $\beta$  and tau

burdens, texture features, and mean signal intensities between *in vivo* Braak stages using analysis of variance (ANOVA) with Bonferroni post-hoc comparisons. We performed all analyses using the Statistical Package for the Social Sciences (SPSS) for Windows (version 22.0; IBM Corporation; Armonk, NY), and considered a two-sided *P* value less than .05 as statistically significant.

## **2. Results**

### **2.1. Associations between MRI texture and A $\beta$ , tau burden**

As summarized in **Table 5**, regional texture features were associated with regional tau burden but not with A $\beta$  burden. The kind of texture features that were associated with tau burden were different between regions. In the hippocampus, autocorrelation was positively associated with tau burden and cluster shade was negatively associated with tau burden. However, neither entropy nor contrast was associated with tau burden. Meanwhile in the PCC, precuneus, and SFC, entropy and contrast were positively associated with tau burden while autocorrelation and cluster shade were not. In the entorhinal cortex, entropy and contrast were positively and cluster shade was negatively associated with tau burden. Mean signal intensity did not show associations with neither A $\beta$  nor tau in all regions.

**Table 5. Associations of the regional texture features with the regional A $\beta$  and tau burdens**

	Entropy		Contrast		Autocorrelation		Cluster Shade		Mean Signal Intensity		
	$\beta$ (95% CI)	<i>p</i>	$\beta$ (95% CI)	<i>p</i>	$\beta$ (95% CI)	<i>p</i>	$\beta$ (95% CI)	<i>p</i>	$\beta$ (95% CI)	<i>p</i>	<i>p</i>
Hippocampus											
A $\beta$ burden	0.05 (-0.15 to 0.25)	0.654	-2.46 (-11.99 to 7.07)	0.654	-27.99 (-56.42 to 0.45)	0.054	81.45 (-240.00 to 402.89)	0.617	0.02 (-0.54 to 0.58)	0.950	
Tau burden	-0.05 (-0.11 to 0.01)	0.118	-1.62 (-4.60 to 1.37)	0.286	<b>21.57</b> <b>(12.66 to 30.47)</b>	<b>&lt;0.001</b>	<b>-285.32</b> <b>(-385.97 to -184.68)</b>	<b>&lt;0.001</b>	0.15 (-0.03 to 0.32)	0.097	
Entorhinal Ctx											
A $\beta$ burden	0.06 (-0.01 to 0.13)	0.078	2.53 (-2.27 to 7.33)	0.299	-3.49 (-11.50 to 4.53)	0.391	28.12 (-37.70 to 93.95)	0.400	0.10 (-0.09 to 0.29)	0.294	
Tau burden	<b>0.04</b> <b>(0.01 to 0.06)</b>	<b>0.003</b>	<b>2.32</b> <b>(0.55 to 4.08)</b>	<b>0.010</b>	2.08 (-0.86 to 5.03)	0.163	<b>-43.30</b> <b>(-67.46 to -19.13)</b>	<b>0.001</b>	0.03 (-0.04 to 0.10)	0.442	
Posterior Cingulate Ctx											
A $\beta$ burden	-0.01 (-0.05 to 0.03)	0.697	0.71 (-1.73 to 3.14)	0.568	1.99 (-4.61 to 8.60)	0.552	-7.98 (-93.77 to 77.82)	0.854	0.08 (-0.07 to 0.23)	0.277	
Tau burden	<b>0.04</b> <b>(0.01 to 0.07)</b>	<b>0.007</b>	<b>2.44</b> <b>(0.71 to 4.18)</b>	<b>0.006</b>	-1.62 (-6.32 to 3.08)	0.497	8.94 (-52.12 to 69.99)	0.773	0.01 (-0.09 to 0.12)	0.812	
Precuneus											
A $\beta$ burden	0.01 (-0.03 to 0.04)	0.625	0.22 (-0.03 to 0.04)	0.834	2.35 (-3.43 to 8.13)	0.423	-32.46 (-79.18 to 14.26)	0.172	0.06 (-0.05 to 0.16)	0.276	
Tau burden	0.03 (0.00 to 0.06)	0.054	<b>1.84</b> <b>(0.00 to 0.06)</b>	<b>0.039</b>	0.79 (-4.16 to 5.74)	0.754	15.76 (-24.22 to 55.74)	0.437	-0.01 (-0.10 to 0.07)	0.748	
Superior Frontal Ctx											
A $\beta$ burden	0.00 (-0.04 to 0.03)	0.818	-1.17 (-3.02 to 0.68)	0.213	-0.41 (-2.83 to 2.02)	0.742	43.91 (-5.19 to 93.01)	0.079	-0.01 (-0.11 to 0.09)	0.848	
Tau burden	<b>0.05</b> <b>(0.00 to 0.10)</b>	<b>0.035</b>	<b>2.99</b> <b>(0.30 to 5.69)</b>	<b>0.029</b>	1.72 (-1.81 to 5.26)	0.337	-44.39 (-115.85 to 27.08)	0.222	0.10 (-0.04 to 0.25)	0.160	

Abbreviations: A $\beta$ , amyloid- $\beta$ ; 95% CI, 95% confidence interval; Ctx, cortex.

Effects of regional A $\beta$  burden and tau burden on regional texture and mean signal intensity, adjusted for age and sex.

## 2.2. Comparisons of AD pathology, MRI texture and mean signal intensity among *in vivo* Braak stage groups

The *in vivo* Braak staging resulted in twelve subjects (2/5 AD, 8/51 MCI, 1/95 NC) being assigned to stage V/VI (Braak V/VI mean SUVR > 1.582), seven (2/5 AD, 3/51 MCI, 3/95 NC) to stage III/VI (Braak III/IV mean SUVR > 0.504), twenty (1/5 AD, 9/51 MCI, 10/95 NC) to stage I/II (Braak I/II mean SUVR > 1.489), and the remaining hundred-twelve (31/51 MCI, 81/95 NC) to stage 0. As the number of subjects assigned to III/IV was too small, we pooled the subjects assigned to stages III/IV and V/VI into stage III/IV/V/VI (n = 19). In all regions, higher Braak stage groups showed higher A $\beta$  and tau burdens, higher entropy, contrast and autocorrelation, and lower cluster shade values compared to lower stage groups (**Table 6** and **Figure 7**). In the hippocampus and entorhinal cortex, the stage I/II and stage III-VI groups showed lower cluster shade and higher entropy and autocorrelation than stage 0. In the entorhinal cortex, stage III-VI groups also had higher entropy and contrast compared to the stage 0 group. In the precuneus, stage I/II and stage III-VI groups showed higher contrast and entropy respectively, than the stage 0 group. However, in the PCC and SFC, all texture features were comparable between Braak stages. Mean signal intensity showed an increasing trend along each Braak stage, but was statistically insignificant in all regions.

**Table 6. Regional A $\beta$  burden, tau burden, and texture features by *in vivo* Braak stages**

	Stage 0 <sup>a</sup> (N =112)	Stage I-II <sup>b</sup> (N = 20)	Stage III-VI <sup>c</sup> (N =19)	Statistics		
				F	P Value	posthoc
<b>Hippocampus</b>						
A $\beta$ burden	0.63 (0.07)	0.67 (0.09)	0.71 (0.07)	10.130	< .001	a < c
Tau burden	1.19 (0.13)	1.57 (0.20)	1.73 (0.32)	102.320	< .001	a < b < c
Entropy	5.80 (0.96)	5.73 (0.91)	5.79 (0.09)	3.511	.032	a < b
Contrast	30.69 (4.80)	30.23 (3.74)	30.37 (4.00)	0.112	.894	--
Autocorrelation	271.71 (9.71)	283.01 (24.91)	279.75 (23.77)	6.464	.002	a < b
Cluster Shade	-74.08 (150.00)	-246.00 (201.76)	-243.83 (208.04)	15.431	<.001	a > b,c
Mean Signal Intensity	2.16 (0.32)	2.19 (0.26)	2.25 (0.26)	0.837	.435	--
<b>Entorhinal Ctx</b>						
A $\beta$ burden	0.56 (0.19)	0.64 (0.27)	0.77 (0.32)	7.473	.001	a < c
Tau burden	1.35 (0.25)	1.86 (0.33)	2.70 (1.06)	79.324	<.001	a < b < c
Entropy	5.90 (0.10)	5.93 (0.07)	5.97 (0.08)	4.884	.009	a < c
Contrast	30.17 (6.87)	33.75 (4.69)	34.65 (5.66)	5.651	.004	a < c
Autocorrelation	267.55 (9.58)	274.84 (13.33)	272.79 (12.32)	5.390	.005	a < b
Cluster Shade	26.80 (81.79)	-83.50 (95.78)	-66.66 (62.04)	22.835	<.001	a > b,c
Mean Signal Intensity	1.96 (0.296)	2.03 (0.24)	2.05 (0.24)	1.350	.262	--
<b>Posterior Cingulate Ctx</b>						
A $\beta$ burden	0.62 (0.25)	0.78 (0.36)	1.13 (0.41)	26.203	<.001	a,b < c
Tau burden	1.08 (0.17)	1.26 (0.15)	2.03 (0.88)	62.772	<.001	a,b < c
Entropy	5.89 (0.07)	5.88 (0.06)	5.92 (0.05)	2.102	.126	--
Contrast	27.99 (4.44)	30.01 (3.50)	30.17 (3.46)	3.568	.031	--
Autocorrelation	266.57 (11.25)	265.01 (6.14)	270.44 (14.34)	1.286	.280	--
Cluster Shade	-14.39 (163.81)	-37.55 (66.83)	-45.63 (73.21)	0.512	.600	--
Mean Signal Intensity	2.11 (0.29)	2.18 (0.25)	2.24 (0.23)	1.790	.171	--
<b>Precuneus</b>						
A $\beta$ burden	0.67 (0.31)	0.86 (0.39)	1.49 (0.50)	44.612	<.001	a,b < c
Tau burden	1.21 (0.15)	1.36 (0.13)	2.16 (1.13)	42.407	<.001	a,b < c
Entropy	5.86 (0.08)	5.89 (0.08)	5.91 (0.09)	4.188	.017	a < c
Contrast	23.41 (4.63)	26.73 (5.17)	26.04 (4.85)	5.884	.003	a < b

Autocorrelation	281.40 (12.87)	281.74 (9.36)	281.75 (15.02)	2.026	.135	--
Cluster Shade	-97.53 (105.15)	-117.87 (107.30)	-112.77 (97.45)	0.434	.649	--
Mean Signal Intensity	1.88 (0.27)	1.95 (0.22)	1.98 (0.21)	1.645	.197	--
Superior Frontal Ctx						
A $\beta$ burden	0.62 (0.29)	0.79 (0.41)	1.28 (0.39)	34.356	<.001	a,b < c
Tau burden	1.17 (0.22)	1.27 (0.12)	1.54 (0.39)	20.699	<.001	a,b < c
Entropy	5.83 (0.07)	5.83 (0.07)	5.85 (0.06)	0.665	.516	--
Contrast	24.68 (4.07)	26.28 (3.76)	25.14 (4.09)	1.355	.261	--
Autocorrelation	269.11 (5.16)	270.18 (2.72)	271.82 (6.53)	2.444	.090	--
Cluster Shade	37.26 (107.96)	-21.30 (84.53)	27.72 (77.99)	2.799	.064	--
Mean Signal Intensity	1.45 (0.23)	1.55 (0.22)	1.52 (0.16)	2.092	.127	--

Mean (standard deviation) are shown for each neuroimaging measure across *in vivo* Braak stages for each region. The mean signal intensity used here is the value derived after normalization to the mean signal intensity of the subject's ventricle. Means across groups were compared using one-way analysis of variance with Bonferroni post hoc comparisons.

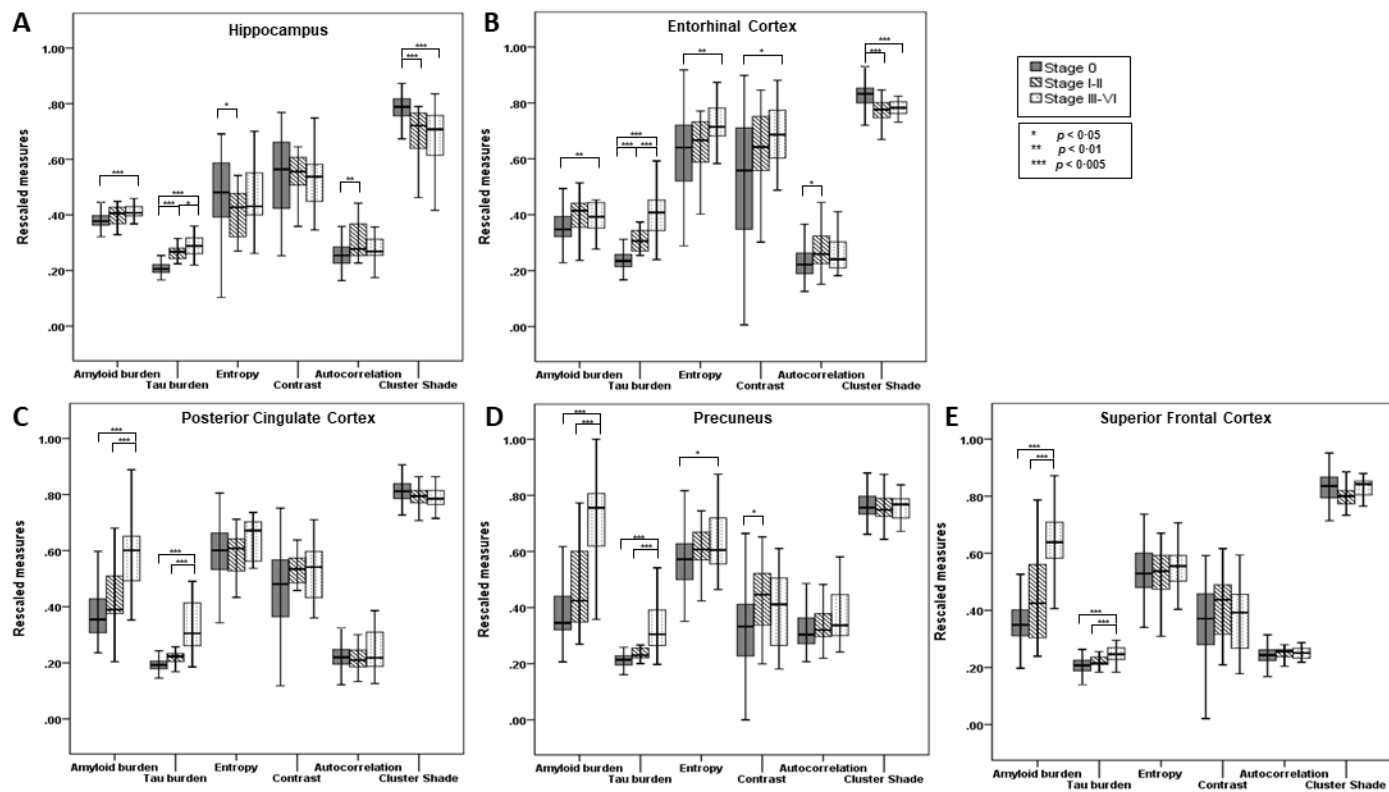


**Figure 7. *In vivo* Braak stage group differences in neuroimaging measures**

Boxplots of neuroimaging metrics across *in vivo* Braak stages are shown for each region (A~E). Neuroimaging metrics have been normalized across all regions from their original values to a scale of 0 to 1, for the purposes of visualization in one graph.

## **IV. Discussion**

## 1. Summary

In the current thesis, I extensively investigated the feasibility of MRI texture as a novel early imaging marker of AD. Ultimately, I aimed to identify a marker that is not only practical (non-invasive and widely accessible) but can also sensitively predict AD in early stages. This was motivated by the need for earlier diagnoses which would lead to more efficient treatments and alleviate the projected socioeconomic burden of AD in the coming years.

In the first part of my research, I focused on exploring the predictive potential of MRI texture, by proposing a new analysis method compared to previous literature. As a result, we found that texture in the hippocampus can discriminate between future AD converters and non-converters in a cohort of heterogeneous MCI patients (**Figure 6A**), better than volume of the hippocampus which is the current gold standard of AD diagnosis. We additionally found that when adding texture from other relevant regions that harbor earlier AD neuropathological proteins (precuneus and PCC), the sensitivity of texture can be further improved. Importantly, texture was able to predict progressors at an earlier time period than volume could, suggesting that texture may reflect microstructural changes that precede atrophy.

In the second part of my research, I investigated what microstructural changes related to AD pathology may underlie the observed predictive power of texture. We discovered that only tau deposition and not A $\beta$  burden is associated with texture, and that the associated texture feature varies depending on the region's cytoarchitecture. Furthermore, texture values

changed with increasing *in vivo* Braak stage. This is a novel and unexpected finding that further delineates the possibility that texture can reflect microstructural changes in the brain tissue.

## 2. MRI texture as an early predictor of AD

In the first study, we defined the control-case population more clearly compared to previous studies and examined the additive value of including other regions of early AD pathology. We demonstrated that the texture of brain MRI is capable of predicting AD progression in MCI patients with an AUC of 0.79 - 0.82 which is, to our knowledge, one of the highest among those reported previously using structural brain MRI from the ADNI. Although this difference may possibly be caused by the differences in field strength and dataset used (1.5T ADNI 1 dataset in most previous studies vs 3T ADNI 2 dataset in our study), the type of texture analysis may be the biggest contributing factor. This study employed second-order statistics (Haralick features) in the texture analysis while previous studies that reported AUCs of 0.67-0.74 in predicting MCI-to-AD conversion employed spectral-based textures (Chincarini et al., 2011; Sørensen et al., 2016). Additionally, it is of note that while there were differences in the number of features and the classification method used for texture and volume, our analyses with non-regularized texture indices provided similar results as the regularized texture indices, showing that the differences in method were not the driving force of the observed differences in accuracies between texture and volume (not shown).

Our study design showed that MRI texture has higher AD predictive power than MRI volume in earlier stages of MCI in particular (**Figure 6B**), and similar performance in later stages of MCI (**Figure 6C**). It is of note that the differences between the two measures across the early

and late stages of MCI are due to the decreased sensitivity of HVI in the former compared to the latter, whereas the sensitivity of texture remains fairly consistent. This suggests that texture may be able to detect early microscopic changes in the brain, before notable neuronal loss occurs, at the timepoint of up to 3 years before progression from MCI to AD.

We also demonstrated the additive benefits of including textures from regions of earlier pathological change other than the hippocampus. While the HTI was marginally more sensitive than the HVI in predicting progression in MCI-PE, CTI was significantly more sensitive than HVI in predicting progression of both MCI-PE and MCI-PL. Even when comparing to a composite index of volume (CVI), CTI was still significantly more sensitive in detecting future progressors in early stage MCI (AUC = 0.817 vs 0.741,  $p = 0.027$ , not shown). This is an interesting result considering that the precuneus and PCC are regions of slightly accelerated atrophy rates near dementia onset (Chételat et al., 2005), and as so the CVI could have yielded higher performance but it remained lower than that of CTI. The precuneus and PCC are also key sites of heavy accumulation of A $\beta$  and reduction of glucose metabolism that begin in very early phases before hippocampal atrophy (Mosconi, 2005). Thus the possibly more accumulated microstructural abnormalities in these regions due to the relatively earlier pathology may have contributed to the additional discriminability of the composite texture compared to the hippocampal texture or volume. While one study did not find texture differences in the precuneus and PCC between AD and NC, the voxelwise texture analysis of the study had employed only one feature per texture map (Maani et al., 2015). Any sole

texture feature of brain MRI would not be sufficient to reflect the complex patterns of neuropathology in the brain.

### **3. MRI texture as a reflection of AD pathology**

While interpretations of what texture reflects should be made with caution in the absence of histological data, there are several candidate mechanisms that have been proposed, such as loss of neuronal cell bodies, changes in structure and density of intracortical myelin, bioaccumulation of iron deposits, and altered water content modulated by altered synaptic density (Westlye et al., 2010). Overall, a combination of these factors in the tissue can lead to a pattern of changes in signal intensity that are subtle and complex.

According to the results of the second study, texture is associated with tau burden, but not with A $\beta$  burden. This selective association with tau in all regions in our study is interesting, considering that tau but not A $\beta$  is known to have a strong association with both brain atrophy and cognitive decline in AD, and that as such tau is a better marker for measuring clinical severity in AD (Hanseeuw et al., 2019; Whitewell et al., 2008; Wood et al., 2019). However, the texture features are more likely to reflect a microstructural change closely associated with tau accumulation rather than the tau proteins per se, because they were not associated with deposition of A $\beta$  proteins, which are much larger than tau. Additionally, higher tau burden was associated with a higher degree of brighter voxels in MRI, as suggested by the decreasing cluster shade values and increasing autocorrelation values and mean signal intensity across all regions.

Although the increase in brighter voxels with increasing AD pathology is in contrast to the intuition that NFT-related neurodegeneration

would form vacuoles that would lead to darker T1w signals, converging evidence on the involvement of myelin-related processes in AD provide a compelling explanation. It has been proposed that AD is a homeostatic response to age-related myelin breakdown (Bartzokis, 2011), in which age-associated unsuccessful attempts to repair myelin results in prolonged axonal swelling and promotes assembly of hyperphosphorylated tau into NFT. Even if myelin repair successfully occurs, the newly formed myelin sheaths are thinner and more susceptible to subsequent insults. This proposal is supported by *in vivo* and *ex vivo* findings of unexpected increases in intracortical myelin content in AD (Bulk et al., 2018; Pelkmans et al., 2019) and in NC with high A $\beta$  burden (Yasuno et al., 2016), and observations of disorganized myeloarchitecture in AD (Bulk et al., 2018; Kenkhuis et al., 2019), a possible result of repetitive myelin repair processes. In *in vivo* neuroimaging studies, higher intracortical myelin content (as measured via T1w/T2w ratio) was associated with higher tau and lower MMSE scores (Pelkmans et al., 2019). In the postmortem MRI-histology studies, late stage AD brains exhibited an inhomogenous, hypointense band throughout the cortex on T2\*w MRI compared to controls, and such hypointense bands blurred the cortical lamination. In addition, T2\*w MRI contrast was correlated most with the spatial distributions of myelin and iron contents rather than with A $\beta$  and tau burdens. The higher myelin and iron contents in the AD brain are suggested to reflect the increased activity of oligodendrocytes, which are the only myelin-forming cells and the most predominant iron-containing cells in the brain. Given that T1w signals are strongly dependent on lipid concentration associated with myelin (Leuze et

al., 2017) and inversely related to T2\*-weighted signals, these studies collectively suggest that the Braak stage-related texture differences observed in our study may have a basis in such myeloarchitectural changes. In light of proposals that myelin changes are at the core of the earliest AD pathological changes (Bartzokis, 2004), imaging methods sensitive to myelin content (i.e. T1w) may be an effective measure for early detection of AD.

In the second study, the type of texture features associated with tau burden also showed a remarkable correspondence with the regional cytoarchitecture (Table 5, Figure 8). The regions in which entropy and contrast were associated with regional tau burden belong to the neocortex (i.e. PCC, precuneus, SFC), which consists of 6 laminae. The hippocampus, in which autocorrelation and cluster shade were associated with regional tau burden, belongs to the allocortex, which consists of 3~4 laminae. The entorhinal cortex, in which entropy, contrast and cluster shade were associated with regional tau burden, belongs to a transitional area between the allocortex and neocortex. This cytoarchitecture-specific pattern in texture-tau associations suggests that each region may have different spatial patterns of tau-related microstructural changes depending on its cytoarchitecture. The three types of cytoarchitecture differ not only in the number of layers but also in the location of cells vulnerable to NFT deposition. NFTs are known to preferentially affect the pyramidal neurons of layers III and V in the neocortex; the stellate neurons of layer II, superficial portion of layer III, and multipolar neurons of layer IV in the entorhinal cortex; and the stratum pyramidale of CA1 and subiculum in the hippocampus (Hyman et al., 1984; Arnold et al., 1991; Braak and Braak,

1991). Consequently, in the neocortical regions which are typically four voxels thick, myelin repair-related processes that are associated with NFTs may selectively change signal intensities of voxels of the inner two rows that correspond to the pyramidal layers. These changes may increase the differences in the MR signal intensities between neighboring inner and outer voxels throughout the neocortical laminae, thus increasing entropy and contrast of the region. Similar but slightly different textural changes may occur in the entorhinal cortex because of the slight difference in the locations of the NFT-affected layers. In the hippocampus, which is a unique structure that consists of rolled-up laminae of its subregions, tau-related microstructural changes along the pyramidal layers that are located laterally may result in an overall lightening and smoothing of the hippocampal signal intensities, thus increasing autocorrelation and decreasing both cluster shade and entropy. A summary of this schema is shown in **Figure 8**.

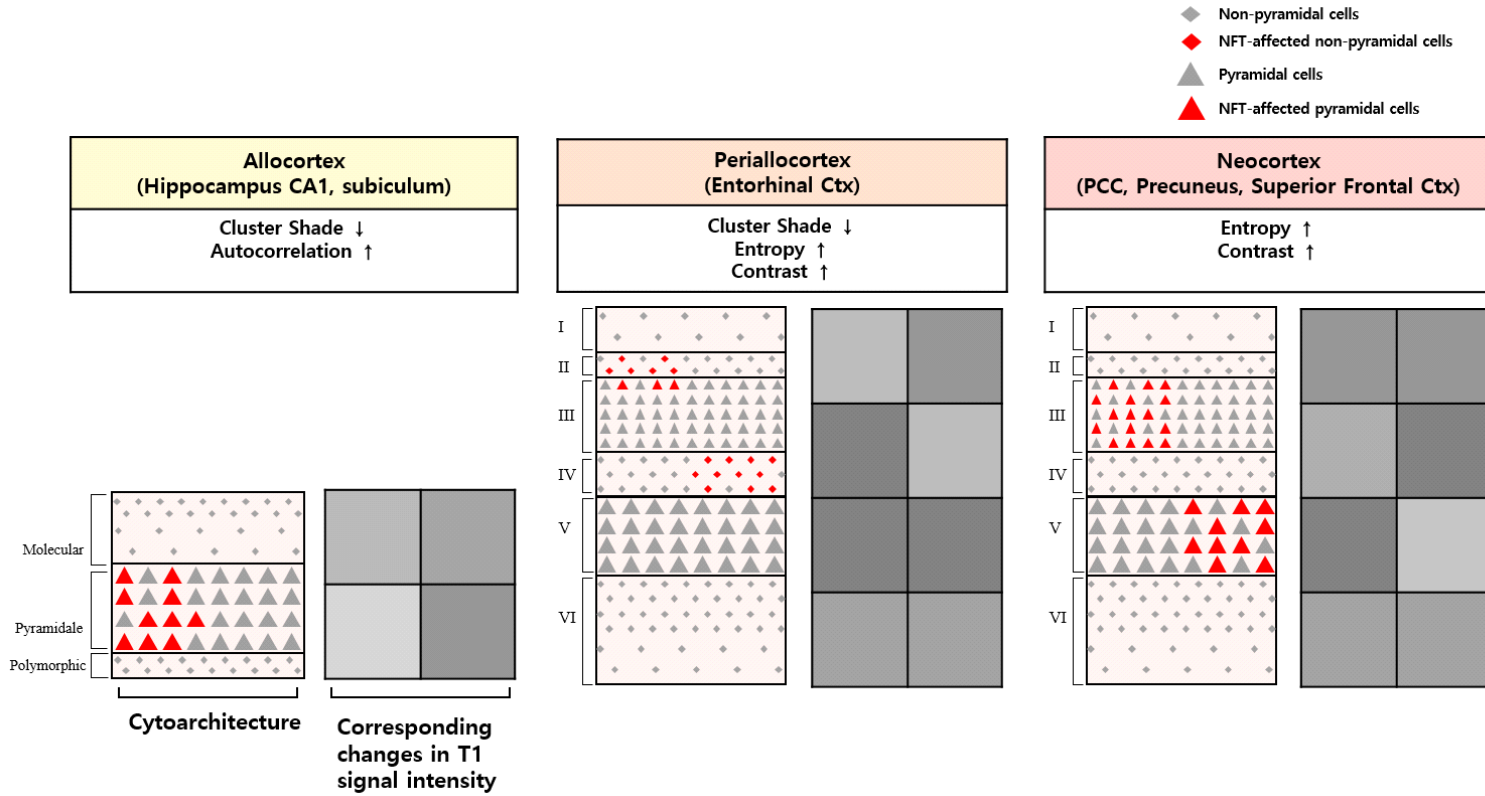


**Figure 8. Schema of texture changes according to cytoarchitecture**

Abbreviations: NFT, neurofibrillary tangle; CA1, cornus ammonis; Ctx, cortex; PCC, posterior cingulate cortex.

#### 4. Advantages and limitations of my research

My two studies were the first, to our knowledge, to specifically compare the predictive value of texture with volume in early and late stages of MCI separately, and to compare texture with AD pathophysiology. The first study revealed the full potential sensitivity of texture in early stages, while the second stage provided insight into what mechanisms may underly the textural differences in early stages. In theory, GM volumetric loss would be observed when there is a reduction in the number of voxels with signal intensities that correspond to GM. Early pathological changes may result in signal intensity changes that are insufficient for the voxel to no longer be classified as GM. This would make first-order features, which depend on the absolute intensity values, less sensitive, while second-order features, which depend on spatial relationships between intensity values, more sensitive. This is notably observed in **Table 5**, where tau is associated with texture features (second-order measures) in all regions but are not associated with mean signal intensity (first-order measures) in any of the regions. However, no individual texture feature alone is expected to be sufficient for accurate discrimination of AD from non-AD. Optimal combinations of relevant texture features, such as the ones from my first study and those from previous literature will be helpful (Sørensen et al., 2016). Furthermore, characterization of the dynamics between texture and volumetric changes through longitudinal studies, as well as testing of textures' predictive validity for incident AD in NC, will be needed.

A potentially confounding factor in texture analysis is the accuracy

of ROI segmentation and noise from adjacent voxels along the boundary between gray matter and white matter. To correct for this, Sorensen et al. removed the surface of hippocampus and only analyzed the interior, resulting in a hippocampus half the original size (Sørensen et al., 2016). In my study, we removed voxels that lie outside the  $\pm 3\sigma$  range, as voxels of another tissue class would likely be among those outliers. MRI field strength can also influence texture analysis to some degree. Magnetic field strength of the MRI scan, which determines signal-to-noise ratio, is another potential confounder, but my study used high-field 3T images, which are more favorable than 1.5 T images used in most other studies.

One limitation of my research is that there were no histological data to validate what is seen through texture. Thus, the myelin-texture association remains a speculation, and future studies on the pathological correlates of texture will be needed to confirm the findings. Another possible limitation is that although texture in the first study showed a consistent trend towards higher performance than volume overall, it is not without risk of Type I error without alpha correction in the AUC comparisons. Also, our second study is limited by the lack of sufficient late-stage AD subjects in our sample, which is partly due to the lack of follow-up data yet accumulated in ADNI 3. Future studies that involve a much larger sample size as well as a more balanced class of not only neuropathological stages but also MRI scanners will be able to validate the findings from both studies.

From a clinical perspective, methods that extract molecular

pathology-related microscopic information from structural MRI are becoming more of value for early detection of AD. The current structural biomarker included in the NIA-AA criteria for AD relies on macroscopic changes that occur too downstream of such microscopic changes. While the utility of structural imaging markers such as texture will depend on the standardization of MRI acquisition methods, the concurrent validity of texture in our study supports previous reports of its potential diagnostic/prognostic use.

## 5. Conclusion and perspectives

Overall, MRI texture demonstrates potential as an early biomarker of AD, both in terms of predictive performance and with correspondence to AD pathology. Texture features of the hippocampus, precuneus, and PCC were able to predict MCI-to-AD progression at an earlier timepoint and at a higher accuracy than hippocampal volume, and texture features in five main regions of AD pathological deposition showed cytoarchitecture-specific associations with tau deposition.

Our results from especially the second study suggest that texture may have uses beyond AD. While further research using myelin data would have to be conducted to confirm, if texture truly reflects myeloarchitectural changes, then it signifies that it is not a marker specific for AD (although it has proven to be a sensitive marker of AD in the first study), but has the potential to be for neurodegenerative diseases in general. Texture may have applications in other neurodegenerative diseases that show different spatial patterns of myelin changes (i.e. differential diagnosis of dementias). So far, texture analysis in medical images have been mostly limited to DCE-MRI for brain tumor images and not as many studies exist for routine clinical images such as T1w images. It will be of great advantage to be able to find possible applications of texture in such routine images for early detection and differential diagnosis. It is hoped that the results of the current thesis led to a further understanding of the pathophysiological mechanisms of AD, as well as provide a lead for more studies of texture analysis applications to other diseases.

## **V. Literature Cited**

- Ahmed, A., et al., 2013. Texture analysis in assessment and prediction of chemotherapy response in breast cancer. *Journal of Magnetic Resonance Imaging*. 38, 89-101.
- Ahmed, M.N., Farag, A.A., 1996. 3D segmentation and labeling using self-organizing Kohonen network for volumetric measurements on brain CT imaging to quantify TBI recovery. In: *Proceedings of 18th Annual International Conference of the IEEE Engineering in Medicine and Biology Society*. Vol. 2, ed.^eds. IEEE, pp. 738-739.
- Albert, M.S., et al., 2011. The diagnosis of mild cognitive impairment due to Alzheimer's disease: Recommendations from the National Institute on Aging-Alzheimer's Association workgroups on diagnostic guidelines for Alzheimer's disease. *Alzheimer's & dementia*. 7, 270-279.
- Albregtsen, F., 2008. Statistical texture measures computed from gray level cooccurrence matrices. *Image processing laboratory, department of informatics, university of oslo*. 5.
- Alonso-Caneiro, D., et al., 2013. Application of texture analysis in tear film surface assessment based on videokeratoscopy. *Journal of Optometry*.
- Antel, S.B., et al., 2003. Automated detection of focal cortical dysplasia lesions using computational models of their MRI characteristics and texture analysis. *Neuroimage*. 19, 1748-1759.
- Arnold, S.E., et al., 1991. The topographical and neuroanatomical distribution of neurofibrillary tangles and neuritic plaques in the cerebral cortex of patients with Alzheimer's disease. *Cerebral cortex*. 1, 103-116.
- Aschenbrenner, A.J., et al., 2018. Influence of tau PET, amyloid PET, and hippocampal volume on cognition in Alzheimer disease. *Neurology*. 91, e859-e866.
- Assefa, D., et al., 2010. Robust texture features for response monitoring of glioblastoma multiforme on-weighted and-FLAIR MR images: A

- preliminary investigation in terms of identification and segmentation. *Medical physics*. 37, 1722-1736.
- Bae, J.B. et al., 2015. Incidence of and risk factors for Alzheimer's disease and mild cognitive impairment in Korean elderly. *Dementia and geriatric cognitive disorders*. 39, 105-115.
- Bartzokis, G., 2004. Age-related myelin breakdown: a developmental model of cognitive decline and Alzheimer's disease. *Neurobiology of Aging*. 25, 5-18.
- Bartzokis, G., 2011. Alzheimer's disease as homeostatic responses to age-related myelin breakdown. *Neurobiology of aging*. 32, 1341-1371.
- Basu, S., et al., 2016. Deep neural networks for texture classification. *Neural Networks & Machine Learning*. 1, 3-3.
- Blacker, D., et al., 1994. Reliability and Validity of NINCDS-ADRDA Criteria for Alzheimer's Disease: The National Institute of Mental Health Genetics Initiative. *Archives of Neurology*. 51, 1198-1204.
- Bonilha, L., et al., 2003. Texture analysis of hippocampal sclerosis. *Epilepsia*. 44, 1546-1550.
- Braak, H., Braak, E., 1991. Neuropathological staging of Alzheimer-related changes. *Acta neuropathologica*. 82, 239-259.
- Braak, H., et al., 2006. Staging of Alzheimer disease-associated neurofibrillary pathology using paraffin sections and immunocytochemistry. *Acta neuropathologica*. 112, 389-404.
- Buch, K., et al., 2018. Quantitative variations in texture analysis features dependent on MRI scanning parameters: A phantom model. *Journal of applied clinical medical physics*. 19, 253-264.
- Bulk, M., et al., 2018. Postmortem MRI and histology demonstrate differential iron accumulation and cortical myelin organization in early- and late-onset Alzheimer's disease. *Neurobiology of Aging*. 62, 231-242.

- Cardenas, V., et al., 2011. Brain atrophy associated with baseline and longitudinal measures of cognition. *Neurobiology of aging*. 32, 572-580.
- Casanova, R., et al., 2011. High Dimensional Classification of Structural MRI Alzheimer's Disease Data Based on Large Scale Regularization. *Frontiers in Neuroinformatics*. 5, 22.
- Casanova, R., et al., 2012. Classification of structural MRI images in Alzheimer's disease from the perspective of ill-posed problems. *PloS one*. 7, e44877.
- Casanova, R., et al., 2013. Alzheimer's disease risk assessment using large-scale machine learning methods. *PloS one*. 8, e77949.
- Chen, W., et al., 2007. Volumetric texture analysis of breast lesions on contrast-enhanced magnetic resonance images. *Magnetic Resonance in Medicine: An Official Journal of the International Society for Magnetic Resonance in Medicine*. 58, 562-571.
- Cherezov, D., et al., 2019. Revealing Tumor Habitats from Texture Heterogeneity Analysis for Classification of Lung Cancer Malignancy and Aggressiveness. *Scientific Reports*. 9, 4500.
- Chételat, G., et al., 2005. Using voxel-based morphometry to map the structural changes associated with rapid conversion in MCI: A longitudinal MRI study. *NeuroImage*. 27, 934-946.
- Chiang, G.C., et al., 2011. Identifying cognitively healthy elderly individuals with subsequent memory decline by using automated MR temporoparietal volumes. *Radiology*. 259, 844-851.
- Chien, Y., Fu, K.-S., 1974. Recognition of X-ray picture patterns. *IEEE Transactions on Systems, Man, and Cybernetics*. 145-156.
- Chincarini, A., et al., 2011. Local MRI analysis approach in the diagnosis of early and prodromal Alzheimer's disease. *NeuroImage*. 58, 469-480.

- Cho, Y., et al., 2012. Individual subject classification for Alzheimer's disease based on incremental learning using a spatial frequency representation of cortical thickness data. *NeuroImage*. 59, 2217-2230.
- Choo, I.H. et al., 2010. Posterior cingulate cortex atrophy and regional cingulum disruption in mild cognitive impairment and Alzheimer's disease. *Neurobiology of aging*. 31, 772-779.
- Christe, S.A., Kumari, B.V., Kandaswamy, A., 2012. Experimental study for 3D statistical property based intracranial brain tumor classification.
- Clausi, D.A., 2002. An analysis of co-occurrence texture statistics as a function of grey level quantization. *Canadian Journal of remote sensing*. 28, 45-62.
- Colgan, N., et al., 2017. In Vivo Imaging of Tau Pathology Using Magnetic Resonance Imaging Textural Analysis. *Frontiers in Neuroscience*. 11.
- Collewet, G., Strzelecki, M., Mariette, F., 2004. Influence of MRI acquisition protocols and image intensity normalization methods on texture classification. *Magnetic Resonance Imaging*. 22, 81-91.
- Connors, R.W., Trivedi, M.M., Harlow, C.A., 1984. Segmentation of a high-resolution urban scene using texture operators. *Computer Vision, Graphics, and Image Processing*. 25, 273-310.
- Convit, A., et al., 1993. Hippocampal atrophy in early Alzheimer's disease: anatomic specificity and validation. *Psychiatric Quarterly*. 64, 371-387.
- Cuingnet, R., et al., 2011. Automatic classification of patients with Alzheimer's disease from structural MRI: a comparison of ten methods using the ADNI database. *NeuroImage*. 56, 766-781.
- Dale, A.M., Sereno, M.I., 1993. Improved localization of cortical activity by combining EEG and MEG with MRI cortical surface reconstruction: a linear approach. *Journal of cognitive neuroscience*. 5, 162-176.
- Dale, A.M., Fischl, B., Sereno, M.I., 1999. Cortical surface-based analysis: I.

- Segmentation and surface reconstruction. *Neuroimage*. 9, 179-194.
- Darling, E.M., Joseph, R.D., 1968. Pattern recognition from satellite altitudes. *IEEE Transactions on Systems Science and Cybernetics*. 4, 38-47.
- Davatzikos, C., et al., 2011. Prediction of MCI to AD conversion, via MRI, CSF biomarkers, pattern classification. *Neurobiology of Aging*. 32, 2322.e19-2322.e27.
- De Leon, M.J., et al., 1996. In Vivo Structural Studies of the Hippocampus in Normal Aging and in Incipient Alzheimer's Disease a. *Annals of the New York Academy of Sciences*. 777, 1-13.
- De Nunzio, G., et al., 2011. A CAD system for cerebral glioma based on texture features in DT-MR images. *Nuclear Instruments and Methods in Physics Research Section A: Accelerators, Spectrometers, Detectors and Associated Equipment*. 648, S100-S102.
- de Oliveira, M.S., et al., 2011. MR imaging texture analysis of the corpus callosum and thalamus in amnesic mild cognitive impairment and mild Alzheimer disease. *American Journal of Neuroradiology*. 32, 60-6.
- DeLong, E.R., DeLong, D.M., Clarke-Pearson, D.L., 1988. Comparing the areas under two or more correlated receiver operating characteristic curves: a nonparametric approach. *Biometrics*. 837-845.
- Deoni, S.C.L., 2010. Quantitative relaxometry of the brain. *Topics in magnetic resonance imaging : TMRI*. 21, 101-113.
- Depeursinge, A., et al., 2007. Lung tissue classification using wavelet frames. In: 2007 29th Annual International Conference of the IEEE Engineering in Medicine and Biology Society. Vol., ed.^eds. IEEE, pp. 6259-6262.
- Depeursinge, A., et al., 2011. Lung texture classification using locally-oriented Riesz components. In: *International Conference on Medical*

- Image Computing and Computer-Assisted Intervention. Vol., ed.^eds. Springer, pp. 231-238.
- Depeursinge, A., et al., 2014. Three-dimensional solid texture analysis in biomedical imaging: review and opportunities. *Medical image analysis*. 18, 176-196.
- Desikan, R.S., et al., 2006. An automated labeling system for subdividing the human cerebral cortex on MRI scans into gyral based regions of interest. *Neuroimage*. 31, 968-980.
- Driscoll, I., Troncoso, J., 2011. Asymptomatic Alzheimer's disease: a prodrome or a state of resilience? *Current Alzheimer Research*. 8, 330-335.
- Dubois, B., et al., 2016. Preclinical Alzheimer's disease: Definition, natural history, and diagnostic criteria. *Alzheimer's & dementia : the journal of the Alzheimer's Association*. 12, 292-323.
- Eliat, P.-A., et al., 2012. Can dynamic contrast-enhanced magnetic resonance imaging combined with texture analysis differentiate malignant glioneuronal tumors from other glioblastoma? *Neurology research international*. 2012.
- Fan, Y., et al., 2008. Spatial patterns of brain atrophy in MCI patients, identified via high-dimensional pattern classification, predict subsequent cognitive decline. *Neuroimage*. 39, 1731-1743.
- Feng, F., et al., 2018. Radiomic Features of Hippocampal Subregions in Alzheimer's Disease and Amnesic Mild Cognitive Impairment. *Frontiers in Aging Neuroscience*. 10.
- Fischl, B., et al., 1999. High-resolution intersubject averaging and a coordinate system for the cortical surface. *Human brain mapping*. 8, 272-284.
- Fischl, B., Dale, A.M., 2000. Measuring the thickness of the human cerebral cortex from magnetic resonance images. *Proceedings of the National*

- Academy of Sciences of the United States of America. 97, 11050-11055.
- Fischl, B., Liu, A., Dale, A.M., 2001. Automated manifold surgery: constructing geometrically accurate and topologically correct models of the human cerebral cortex. *IEEE transactions on medical imaging*. 20, 70-80.
- Fischl, B., et al., 2002. Whole brain segmentation: automated labeling of neuroanatomical structures in the human brain. *Neuron*. 33, 341-355.
- Fischl, B., et al., 2004a. Sequence-independent segmentation of magnetic resonance images. *Neuroimage*. 23, S69-S84.
- Fischl, B., et al., 2004b. Automatically parcellating the human cerebral cortex. *Cerebral cortex*. 14, 11-22.
- Fox, N., et al., 1996. Presymptomatic hippocampal atrophy in Alzheimer's disease: A longitudinal MRI study. *Brain*. 119, 2001-2007.
- Freeborough, P.A., Fox, N.C., 1998. MR image texture analysis applied to the diagnosis and tracking of Alzheimer's disease. *IEEE Transactions on Medical Imaging*. 17, 475-478.
- Friedman, J., Hastie, T., Tibshirani, R., 2010. Regularization Paths for Generalized Linear Models via Coordinate Descent. *Journal of Statistical Software* 33, 1-22.
- Frisoni, G.B., et al., 2010. The clinical use of structural MRI in Alzheimer disease. *Nature Reviews: Neurology*. 6, 67-77.
- Gensheimer, M.F., et al., 2015. Assessing the scale of tumor heterogeneity by complete hierarchical segmentation of MRI. *Physics in Medicine & Biology*. 60, 977.
- Georgiadis, P., et al., 2009. Enhancing the discrimination accuracy between metastases, gliomas and meningiomas on brain MRI by volumetric textural features and ensemble pattern recognition methods. *Magnetic resonance imaging*. 27, 120-130.

- Gerardin, E., et al., 2009. Multidimensional classification of hippocampal shape features discriminates Alzheimer's disease and mild cognitive impairment from normal aging. *Neuroimage*. 47, 1476-1486.
- Goldbach, M., Menhardt, W., Stevens, J., 1991. Multispectral tissue characterization in magnetic resonance imaging using bayesian estimation and markov random fields. In: *Proceedings of the Annual International Conference of the IEEE Engineering in Medicine and Biology Society Volume 13: 1991*. Vol., ed.^eds. IEEE, pp. 62-63.
- Goubran, M., et al., 2015. Magnetic resonance imaging and histology correlation in the neocortex in temporal lobe epilepsy. *Annals of Neurology*. 77, 237-250.
- Gowland, P.A., Stevenson, V.L., 2004. T1: The Longitudinal Relaxation Time. In: *Quantitative MRI of the Brain*. Vol., ed.^eds. John Wiley & Sons, Ltd, pp. 111-141.
- Greve, D.N., et al., 2016. Different partial volume correction methods lead to different conclusions: An 18F-FDG-PET study of aging. *Neuroimage*. 132, 334-343.
- Guillozet, A.L., et al., 2003. Neurofibrillary Tangles, Amyloid, and Memory in Aging and Mild Cognitive Impairment. *Archives of Neurology*. 60, 729-736.
- Hall-Beyer, M., 2000. GLCM texture: a tutorial. *National Council on Geographic Information and Analysis Remote Sensing Core Curriculum*. 3.
- Hall, E.L., et al., 1971. A survey of preprocessing and feature extraction techniques for radiographic images. *IEEE Transactions on Computers*. 100, 1032-1044.
- Han, J.W. et al., 2012. Predictive validity and diagnostic stability of mild cognitive impairment subtypes. *Alzheimer's & dementia : the journal of the Alzheimer's Association*. 8, 553-559.

- Han, J.W. et al., 2012a. Multimodal Cognitive Enhancement Therapy for Patients with Mild Cognitive Impairment and Mild Dementia: A Multi- Center, Randomized, Controlled, Double-Blind, Crossover Trial. *J Alzheimers Dis.* 55(2), 787-796
- Han, J.W. et al., 2012b. Efficacy of the Ubiquitous Spaced Retrieval-based Memory Advancement and Rehabilitation Training (USMART) program among patients with mild cognitive impairment: a randomized controlled crossover trial. *Alzheimers Res Ther.* 9(1), 39
- Hanseeuw, Bernard J., et al. "Association of Amyloid and Tau With Cognition in Preclinical Alzheimer Disease: A Longitudinal Study." *JAMA neurology* (2019).
- Haralick, R.M., Shanmugam, K., Dinstein, I.h., 1973. Textural features for image classification. *IEEE Transactions on Systems, Man and Cybernetics.* 610-621.
- Hu, L.S., et al., 2015. Multi-Parametric MRI and Texture Analysis to Visualize Spatial Histologic Heterogeneity and Tumor Extent in Glioblastoma. *PLoS ONE.* 10, e0141506.
- Hyman, B.T., et al., 1984. Alzheimer's disease: cell-specific pathology isolates the hippocampal formation. *Science.* 225, 1168.
- Jack, C.R., et al., 1992. MR-based hippocampal volumetry in the diagnosis of Alzheimer's disease. *Neurology.* 42, 183-183.
- Jack, C.R., et al., 2010. Hypothetical model of dynamic biomarkers of the Alzheimer's pathological cascade. *Lancet neurology.* 9, 119.
- Jafari-Khouzani, K., et al., 2004. Comparison of 2D and 3D wavelet features for TLE lateralization. In: *Medical Imaging 2004: Physiology, Function, and Structure from Medical Images.* Vol. 5369, ed.^eds. International Society for Optics and Photonics, pp. 593-601.
- Jiang, G., Wang, X., Tong, L., 2010. Study of Correlation between Hippocampus's Texture and Morphological Features in Alzheimer's

- Disease Patients Based on MR Image. In: World Congress on Medical Physics and Biomedical Engineering, September 7 - 12, 2009, Munich, Germany: Vol. 25/4 Image Processing, Biosignal Processing, Modelling and Simulation, Biomechanics. Vol., O. Dössel, W.C. Schlegel, ed.^eds. Springer Berlin Heidelberg, Berlin, Heidelberg, pp. 1908-1911.
- Jhoo, J.H. et al., 2008. Prevalence of dementia and its subtypes in an elderly urban korean population: results from the Korean Longitudinal Study on Health And Aging (KLoSHA). *Dementia and geriatric cognitive disorders*. 26, 270-276.
- Kaizer, H., 1955. A quantification of textures on aerialphotographs. Boston University Research Laboratories, Boston University, Tech. Note.
- Kantarci, K., et al., 2005. DWI PREDICTS FUTURE PROGRESSION TO ALZHEIMER'S DISEASE IN AMNESTIC MILD COGNITIVE IMPAIRMENT. *Neurology*. 64, 902-904.
- Kassner, A., Thornhill, R.E., 2010. Texture analysis: a review of neurologic MR imaging applications. *AJNR Am J Neuroradiol*. 31, 809-16.
- Keifer Jr, O.P., et al., 2015. Voxel-based morphometry predicts shifts in dendritic spine density and morphology with auditory fear conditioning. *Nature Communications*. 6, 7582.
- Kenkhuis, B., et al., 2019. 7T MRI allows detection of disturbed cortical lamination of the medial temporal lobe in patients with Alzheimer's disease. *NeuroImage: Clinical*. 21, 101665.
- Kessler, R.C., et al., 2015. Predicting suicides after psychiatric hospitalization in US Army soldiers: the Army Study to Assess Risk and Resilience in Servicemembers (Army STARRS). *JAMA Psychiatry*. 72, 49-57.
- Kim, K.W. et al., 2011. A nationwide survey on the prevalence of dementia and mild cognitive impairment in South Korea. *Journal of Alzheimer's disease : JAD*. 23, 281-291.

- Kim, Y.J. et al., 2014. Prevalence and trends of dementia in Korea: a systematic review and meta-analysis. *Journal of Korean medical science*. 29, 903-912.
- Kurz, A. et al., 2009. Cognitive rehabilitation in patients with mild cognitive impairment. *Int J Geriatr Psychiatry*. 24, 163-168.
- Landau, S.M., et al., 2012. Amyloid deposition, hypometabolism, and longitudinal cognitive decline. *Annals of neurology*. 72, 578-586.
- Larroza, A., Bodí, V., Moratal, D., 2016. Texture Analysis in Magnetic Resonance Imaging: Review and Considerations for Future Applications. In: *Assessment of Cellular and Organ Function and Dysfunction using Direct and Derived MRI Methodologies*. Vol., ed.^eds. InTech.
- LeCun, Y., Bengio, Y., 1995. Convolutional networks for images, speech, and time series. *The handbook of brain theory and neural networks*. 3361, 1995.
- Lee, S., Lee, H., Kim, K., 2019. Magnetic resonance imaging texture predicts progression to dementia due to Alzheimer disease earlier than hippocampal volume. *Journal of Psychiatry & Neuroscience: JPN*. 44, 1-8.
- Lerski, R., et al., 1979. Computer analysis of ultrasonic signals in diffuse liver disease. *Ultrasound in medicine & biology*. 5, 341-343.
- Leung, T., Malik, J., 2001. Representing and recognizing the visual appearance of materials using three-dimensional textons. *International journal of computer vision*. 43, 29-44.
- Leuze, C., et al., 2017. The separate effects of lipids and proteins on brain MRI contrast revealed through tissue clearing. *Neuroimage*. 156, 412-422.
- Li, I.I. et al., 2011. Cognitive intervention for persons with mild cognitive impairment: A meta-analysis. *Ageing Res Rev*. 10, 285-296.

- Linfoot, E.H., 1957. An informational measure of correlation. *Information and control*. 1, 85-89.
- Livens, S., et al., 1997. Wavelets for texture analysis, an overview.
- Lopes, R., et al., 2011a. Prostate cancer characterization on MR images using fractal features. *Medical physics*. 38, 83-95.
- Lopes, R., et al., 2011b. Local fractal and multifractal features for volumic texture characterization. *Pattern Recognition*. 44, 1690-1697.
- Luk, C.C., et al., 2018. Alzheimer's disease: 3-Dimensional MRI texture for prediction of conversion from mild cognitive impairment. *Alzheimer's & dementia (Amsterdam, Netherlands)*. 10, 755-763.
- Maani, R., Yang, Y.H., Kalra, S., 2015. Voxel-based texture analysis of the brain. *PLoS One*. 10, e0117759.
- Maarouf, C.L., et al., 2014. Biochemical assessment of precuneus and posterior cingulate gyrus in the context of brain aging and Alzheimer's disease. *PloS one*. 9, e105784.
- Madabhushi, A., et al., 2003. A novel stochastic combination of 3D texture features for automated segmentation of prostatic adenocarcinoma from high resolution MRI. In: *International Conference on Medical Image Computing and Computer-Assisted Intervention*. Vol., ed.^eds. Springer, pp. 581-591.
- Mahmoud-Ghoneim, D., et al., 2008. The impact of image dynamic range on texture classification of brain white matter. *BMC medical imaging*. 8, 18.
- Marmol, U., 2011. Use of Gabor filters for texture classification of airborne images and LIDAR data. *Archiwum Fotogrametrii, Kartografii i Teledetekcji*. 22.
- Mathias, J., Tofts, P., Losseff, N., 1999. Texture analysis of spinal cord pathology in multiple sclerosis. *Magnetic Resonance in Medicine: An Official Journal of the International Society for Magnetic Resonance*

- in Medicine. 42, 929-935.
- Mattsson, N., et al., 2019. Staging  $\beta$ -Amyloid Pathology With Amyloid Positron Emission Tomography. *JAMA Neurology*.
- Mayerhoefer, M.E., et al., 2010. Texture-based classification of focal liver lesions on MRI at 3.0 Tesla: A feasibility study in cysts and hemangiomas. *Journal of Magnetic Resonance Imaging*. 32, 352-359.
- Mosconi, L., 2005. Brain glucose metabolism in the early and specific diagnosis of Alzheimer's disease. FDG-PET studies in MCI and AD. *Eur J Nucl Med Mol Imaging*. 32, 486-510.
- Nagarajan, M.B., et al., 2013. Classification of small lesions in dynamic breast MRI: eliminating the need for precise lesion segmentation through spatio-temporal analysis of contrast enhancement. *Machine vision and applications*. 24, 1371-1381.
- Nanni, L., et al., 2019. Texture descriptors and voxels for the early diagnosis of Alzheimer's disease. *Artificial Intelligence in Medicine*. 97, 19-26.
- Nelson, P.T., et al., 2012. Correlation of Alzheimer disease neuropathologic changes with cognitive status: a review of the literature. *Journal of neuropathology and experimental neurology*. 71, 362-381.
- Nie, K., et al., 2008. Quantitative analysis of lesion morphology and texture features for diagnostic prediction in breast MRI. *Academic radiology*. 15, 1513-1525.
- Ojala, T., Pietikainen, M., Harwood, D., 1994. Performance evaluation of texture measures with classification based on Kullback discrimination of distributions. In: *Proceedings of 12th International Conference on Pattern Recognition*. Vol. 1, ed.^eds. IEEE, pp. 582-585.
- Ortiz, A., et al., 2013. Segmentation of brain MRI using SOM-FCM-based method and 3D statistical descriptors. *Computational and mathematical methods in medicine*. 2013.

- Palmqvist, S., et al., 2017. Earliest accumulation of  $\beta$ -amyloid occurs within the default-mode network and concurrently affects brain connectivity. *Nature communications*. 8, 1214.
- Pelkmans, W., et al., 2019. Gray matter T1-w/T2-w ratios are higher in Alzheimer's disease. *Human Brain Mapping*. 40, 3900-3909.
- Petersen, R.C., et al., 2001. Current Concepts in Mild Cognitive Impairment. *Archives of Neurology*. 58, 1985-1992.
- Petersen, R.C., et al., 2005. Vitamin E and Donepezil for the Treatment of Mild Cognitive Impairment. *New England Journal of Medicine*. 352, 2379-2388.
- Prasanna, P., Tiwari, P., Madabhushi, A., 2014. Co-occurrence of Local Anisotropic Gradient Orientations (CoLIAGe): distinguishing tumor confounders and molecular subtypes on MRI. In: *International Conference on Medical Image Computing and Computer-Assisted Intervention*. Vol., ed.^eds. Springer, pp. 73-80.
- Prince, M., et al., 2015. The global impact of dementia: an analysis of prevalence, incidence, cost and trends. *World Alzheimer Report*. 2015.
- Qian, J.H., T.; Friedman, J.; Tibshirani, R.; Simon, N, 2013. *Glmnet for Matlab*.
- Ramusino, M.C., et al., 2019. Incremental value of amyloid-PET versus CSF in the diagnosis of Alzheimer's disease. *European journal of nuclear medicine and molecular imaging*. 1-11.
- Schmierer, K., et al., 2010. High field (9.4 Tesla) magnetic resonance imaging of cortical grey matter lesions in multiple sclerosis. *Brain*. 133, 858-867.
- Schneider, L.S., et al., 2014. Clinical trials and late-stage drug development for Alzheimer's disease: an appraisal from 1984 to 2014. *Journal of internal medicine*. 275, 251-283.

- Schöll, M., et al., 2016. PET imaging of tau deposition in the aging human brain. 89, 971-982.
- Ségonne, F., et al., 2004. A hybrid approach to the skull stripping problem in MRI. *Neuroimage*. 22, 1060-1075.
- Ségonne, F., Pacheco, J., Fischl, B., 2007. Geometrically accurate topology-correction of cortical surfaces using nonseparating loops. *IEEE transactions on medical imaging*. 26, 518-529.
- Shafer, C.M., Seewaldt, V.L., Lo, J.Y., 2011. Validation of a 3D hidden-Markov model for breast tissue segmentation and density estimation from MR and tomosynthesis images. In: *Proceedings of the 2011 Biomedical Sciences and Engineering Conference: Image Informatics and Analytics in Biomedicine*. Vol., ed.^eds. IEEE, pp. 1-4.
- Simões, R., Slump, C., Walsum, A.M.v.C.v., 2012. Using local texture maps of brain MR images to detect Mild Cognitive Impairment. In: *Proceedings of the 21st International Conference on Pattern Recognition (ICPR2012)*. Vol., ed.^eds., pp. 153-156.
- Sled, J.G., Zijdenbos, A.P., Evans, A.C., 1998. A nonparametric method for automatic correction of intensity nonuniformity in MRI data. *IEEE transactions on medical imaging*. 17, 87-97.
- Soh, L.-K., Tsatsoulis, C., 1999. Texture analysis of SAR sea ice imagery using gray level co-occurrence matrices. *IEEE Transactions on geoscience and remote sensing*. 37, 780-795.
- Sørensen, L., et al., 2016. Early Detection of Alzheimer's Disease Using MRI Hippocampal Texture. *Human Brain Mapping*. 37, 1148-1161.
- Strzelecki, M., Lee, M., 2011. Analysis of three-dimensional magnetic resonance human liver images. *IETE Journal of Research*. 57, 237-245.
- Tatsuoka, C., et al., 2013. Modeling the heterogeneity in risk of progression

- to Alzheimer's disease across cognitive profiles in mild cognitive impairment. *Alzheimer's research & therapy*. 5, 14-14.
- Thompson, P.M., et al., 2004. Mapping hippocampal and ventricular change in Alzheimer disease. *Neuroimage*. 22, 1754-1766.
- Ulaby, F.T., et al., 1986. Textural Information in SAR Images. *IEEE Transactions on Geoscience and Remote Sensing*. GE-24, 235-245.
- van Griethuysen, J.J.M., et al., 2017. Computational Radiomics System to Decode the Radiographic Phenotype. *Cancer research*. 77, e104-e107.
- Vemuri, P., et al., 2008. Antemortem MRI based STructural Abnormality iNDex (STAND)-scores correlate with postmortem Braak neurofibrillary tangle stage. *Neuroimage*. 42, 559-567.
- Visser, P.J., et al., 2002. Medial temporal lobe atrophy predicts Alzheimer's disease in patients with minor cognitive impairment. *Journal of neurology, neurosurgery, and psychiatry*. 72, 491-497.
- Westlye, L.T., et al., 2010. Differentiating maturational and aging-related changes of the cerebral cortex by use of thickness and signal intensity. *NeuroImage*. 52, 172-185.
- Weston, P.S.J., et al., 2015. Diffusion imaging changes in grey matter in Alzheimer's disease: a potential marker of early neurodegeneration. *Alzheimer's Research & Therapy*. 7, 47.
- Whitwell, J.L., et al., 2008. MRI correlates of neurofibrillary tangle pathology at autopsy: a voxel-based morphometry study. *Neurology*. 71, 743-749.
- Wood, H. (2019). Sequential amyloid- $\beta$  and tau accumulation foreshadows cognitive decline. *Nature Reviews Neurology*.doi:10.1038/s41582-019-0230-0
- Wu, J., et al., 2016. Intratumor partitioning and texture analysis of dynamic contrast-enhanced (DCE)-MRI identifies relevant tumor subregions to predict pathological response of breast cancer to neoadjuvant

- chemotherapy. *Journal of Magnetic Resonance Imaging*. 44, 1107-1115.
- Xia, H., et al., 2012. Texture Analysis and Volumetry of Hippocampus and Medial Temporal Lobe in Patients with Alzheimer's Disease. In: 2012 International Conference on Biomedical Engineering and Biotechnology. Vol., ed.^eds., pp. 905-908.
- Yasuno, F., et al., 2016. Use of T1-weighted/T2-weighted magnetic resonance ratio to elucidate changes due to amyloid  $\beta$  accumulation in cognitively normal subjects. *NeuroImage. Clinical*. 13, 209-214.
- Yokoi, T., et al., 2018. Involvement of the Precuneus/Posterior Cingulate Cortex Is Significant for the Development of Alzheimer's Disease: A PET (THK5351, PiB) and Resting fMRI Study. *Frontiers in aging neuroscience*. 10, 304-304.
- Zacharaki, E.I., et al., 2009. Classification of brain tumor type and grade using MRI texture and shape in a machine learning scheme. *Magnetic Resonance in Medicine*. 62, 1609-1618.
- Zhang, J., Wang, L., Tong, L., 2007. Feature reduction and texture classification in MRI-Texture analysis of multiple sclerosis. In: 2007 IEEE/ICME International Conference on Complex Medical Engineering. Vol., ed.^eds. IEEE, pp. 752-757.
- Zhang, J., et al., 2008. Texture analysis of multiple sclerosis: a comparative study. *Magnetic Resonance Imaging*. 26, 1160-1166.
- Zhang, Y., 2012. MRI Texture Analysis in Multiple Sclerosis. *International Journal of Biomedical Imaging*. 2012, 7.

## 국문 초록

### 알츠하이머병 조기진단 지표로서 자기공명영상 질감에 대한 연구

서울대학교 대학원

뇌인지과학과

이수빈

알츠하이머병은 (AD) 현재 치료방법이 없는 신경퇴행성 질환이나, 초기에 치료제를 투여할수록 효과를 나타내므로 조기진단하는 것이 매우 중요하다. 질감 분석은 이미지 내 신호밝기의 공간적 분포도의 패턴을 수치화하는 방법으로, 몇몇 연구에 따라 AD의 초기 바이오마커로서의 가능성이 제기되어왔다. 본 학위논문에서는 AD 조기진단 지표로서 자기공명영상(MRI) 질감의 타당성과 기전을 보는 연구들로 구성되어 있다.

첫 번째 연구는 AD 진단 및 예측 도구로서 MRI 복합텍스처를 개발 후 그 성능을 분석한 연구이다. 그 결과, AD환자와 정상인지노인을 90%이상의 정확도로 분류할 수 있었고, 경도인지장애환자 중 3년 이내로 AD로 전환할 초기 및 말기 단계 환자를 약 80%의 정확도로 예측할 수 있는 것으로 확인했다. 또한 이는 종래 방법 (해마 용적)보다 더 초기 단계에서 더 높은 성능을 보였다.

두 번째 연구는 MRI 질감이 AD 병리의 어떤 측면을 반영하는지 본 연구이다. 초기와 중기 단계에 AD 주요 병리가 축적되는 5개 뇌 영역에서 아밀로이드와 타우 단백질 양이 텍스처에 미치는 영향을 분석했다. 분석 결과, 영역 별 타우 단백질의 축적량만 텍스처에 영향을 미쳤지만, 뇌 영역의 세포구축 (cytoarchitecture)에 따라 다른 텍스처 피처를 변화시키는 것으로 확인했다. 구체적으로, 신생피질(neocortex)에 해당되는 뇌 영역에서는 타우 축적량이 entropy와 contrast와 연관성을 보였고, 이종피질 (allocortex)에 해당되는 뇌 영역에서는 autocorrelation과 cluster shade와 연관성을 보였다.

결론적으로 본 논문은 MRI 질감이 AD의 조기진단 지표로서의 가능성에 대한 증거를 제시한다.

주요어: 알츠하이머병, 자기공명영상, 질감, 바이오마커, 뇌영상, 조기진단, 예측, 병리, 검증

학 번: 2014-25135